ELSEVIER

Astroparticle Physics 16 (2001) 13–46

Astroparticle Physics

www.elsevier.com/locate/astropart

Composition and energy spectra of cosmic-ray primaries in the energy range 10^{13}–10^{15} eV/particle observed by Japanese–Russian joint balloon experiment

RUNJOB Collaboration [1]

A.V. Apanasenko [a], V.A. Sukhadolskaya [b], V.A. Derbina [b], M. Fujii [c], V.I. Galkine [b], G.G. Getsov [d], M. Hareyama [e], M. Ichimura [f], S. Ito [f], E. Kamioka [g], T. Kitami [f], T. Kobayashi [e], V.D. Kolesnikov [h], V. Kopenkin [d], N.M. Kotunova [a], S. Kuramata [f], Y. Kuriyama [e], V.I. Lapshin [a,2], A.K. Managadze [d], H. Matsutani [i], H. Mikami [f], N.P. Misnikova [a], R.A. Mukhamedshin [j], M. Namiki [k], H. Nanjo [f], S.N. Nazarov [b], S.I. Nikolsky [a], T. Ohe [e], S. Ohta [k], V.I. Osedlo [b], D.S. Oshuev [d], D.M. Podorozhny [d], P.A. Publichenko [b], I.V. Rakobolskaya [b], T.M. Roganova [d], M. Saito [e], G.P. Sazhina [d], H. Semba [m], Yu.N. Shabanova [b], T. Shibata [e,*], H. Sugimoto [l], L.G. Sveshnikova [d], K. Takahashi [e], T. Tsuchiya [f], V.M. Taran [h], N. Yajima [k], T. Yamagami [k], K. Yamamoto [e], I.V. Yashin [d], E.A. Zamchalova [d], G.T. Zatsepin [j], I.S. Zayarnaya [a]

[a] *P.N. Lebedev Physical Institute of Russian Academy of Sciences, Moscow 117924, Russia*
[b] *Physical Department of Moscow State University, Moscow 119899, Russia*
[c] *Faculty of Engineering, Aomori University, Aomori 030-0943, Japan*
[d] *D.V. Skobeltsyn Institute of Nuclear Physics, Moscow State University, Moscow 119899, Russia*
[e] *Department of Physics, Aoyama Gakuin University, Tokyo 157-8572, Japan*
[f] *Faculty of Science and Technology, Hirosaki University, Hirosaki 036-8561, Japan*
[g] *Multimedia Information Research Division, National Institute of Informatics, The Ministry of Education, Tokyo 101-8430, Japan*
[h] *Volsk Expeditionary Base of P.N. Lebedev Physical Institute, Volsk 412680, Russia*
[i] *School of Medicine, Hirosaki University, Hirosaki 036-8562, Japan*
[j] *Institute for Nuclear Researches of Russian Academy of Sciences, Moscow 117312, Russia*
[k] *Institute of Space and Astronautical Science, Sagamihara 229-8510, Japan*

[*] Corresponding author.

[1] RUssia–Nippon JOint Balloon-program.

[2] Professor V.I. Lapshin passed away on 13 July 2000 in the process of revising the present paper. Without his great effort in organizing everything related to ballooning operations, the present joint experiment would not be realized. We pray heartily for the repose of his soul.

0927-6505/01/$ - see front matter
PII: S0927-6505(00)00163-8

[1] Shonan Institute of Technology, Fujisawa 251-8511, Japan
[m] Department of Management, Urawa College, Urawa 337-0974, Japan

Received 29 February 2000; received in revised form 30 August 2000; accepted 28 September 2000

Abstract

We report experimental results obtained by the emulsion chambers on board of the long duration balloon. We have been carrying out the trans-Siberian-continental balloon flight since 1995, and the results from 1995 to 1996 experiments are presented here. Total exposure of these two years amounts to 231.5 m^2 h at the average altitude of ~32 km.

The energy range covers 10–500 TeV for proton-primary, 3–70 TeV/n for helium-primary, and 1–5 TeV/n for Fe-group ($Z = 26$–28), though statistics of heavy components is not yet enough. Our preliminary data show that the spectra of the proton and the helium have nearly the same power indices ~2.80, while those of heavier ones become gradually harder as the mass gets heavier, for instance the index is ~2.70 for CNO-group and ~2.55 for Fe-group.

It is remarkable that a very high energy proton with multi-PeV is detected in 1995 experiment, and the estimated flux of this event coincides with a simple extrapolation from the energy spectrum with the power index 2.8 observed in the range 10–500 TeV. It indicates that there is no spectral break at around 100 TeV, in contrast to the maximum energy predicted by the current shock-wave acceleration model. This evidence requires some modification on the acceleration and/or propagation mechanism.

Also we present all-particle spectrum and the average primary mass in the energy range 20–1000 TeV/particle. Our preliminary data show no drastic change in mass composition over the wide energy range, at least up to 1 PeV/particle, though the statistics is not yet enough to confirm it concretely.

The flight performance and the procedure of the analysis, particularly the energy determination methods and the detection efficiency calculation are also given.

1. Introduction

Nowadays, the energy spectrum of cosmic-rays extends up to more than 10^{20} eV, well beyond the so-called Greisen–Zatsepin–Kuzmin cut-off energy [1,2]. Nevertheless, we do not reach yet a common consensus on the origin and the acceleration mechanism of cosmic-rays even below $\sim 10^{18}$ eV, the confinement energy in our galaxy. Above all, the "knee" puzzle is still left behind, although first signal of the knee was observed by Kulikov and Khristiansen [3] more than 40 years ago, and Peters [4] immediately pointed out its importance in understanding of the origin of galactic cosmic radiation.

Though many theorists have developed an attractive theory of diffusive shock acceleration by supernova blast waves [5–7], and succeeded in accounting for the observational data of the cosmic-ray particles in the lower energy region, $\lesssim 10$ TeV, the current theory cannot accelerate protons beyond ~100 TeV, mainly due to a finite lifetime of the shock waves: that is in marked contrast with the observational data. In fact, we detect a proton primary with the energy as high as multi-PeV in the first balloon experiment of 1995 (see Section 4.2 in this paper).

To solve the difficulty in the acceleration limit at $E_{max} \sim 100$ TeV for proton, several theorists have proposed other models, involving mechanism such as a postacceleration [8,9] after the energy gain by the direct shock acceleration in supernova remnants (SNR's), or introducing a new source [10–12] to reproduce a "bump" appeared around the knee, [3] and so on [13–15].

Each model predicts a somewhat different feature in the composition near the knee. For instance, Axford [8,9] proposes that the cosmic-ray components above the knee are primarily the same as

[3] Recent air shower experiments [53,54] show, however, no significant "bump" around the knee, but a rather smooth change of the slope in the all-particle spectrum between below and above the knee, say from ~2.7 to ~3.1.

those below the knee, and the energy spectrum of the latter with the cut-off at ZE_{max} (Z: charge of the primary element) is boosted well above the knee region, $\gtrsim 1$ PeV, due to the multiple collision with large scale shock-waves in the interstellar medium. Therefore the average mass of the primary elements does not change so drastically around the knee region, but increases rather slowly at higher energies, similarly as observed below the knee.

Alternatively, several authors [10–12] propose that some "new" component might give rise to the recovery in the energy spectrum above the knee. In this case, we expect the composition changes *drastically* either into heavier one or into lighter one above the knee, which depends on the type of new source.

On the other hand some author [16] claims from another point of view that the knee is not caused by the astrophysical origin mentioned above, but by a fundamental change in the nuclear interaction at very high energies, $\gtrsim 100$ TeV. One may comment that such a possibility is absolutely rejected because the recent accelerator results show no drastic change in the multiple meson production at the energies of 100–1000 TeV [17]. But such a comment is not acceptable so straightforwardly, since these data are based on the collider machine and no definite data are available in the forward region, where the behaviour of the fast secondaries is most important for the development of shower phenomena in the atmosphere. However, we do not touch this problem here as it is slightly deviated from the objective of the present paper, but one should always keep such a possibility in mind.

Anyway, a key to confirm which model is correct is to establish *directly* the chemical composition in the knee region. It is, however, not so easy to make clear the composition in the knee region from the direct observational method, and the energy region above 10^{14} eV/particle has been basically covered by the ground-based air shower experiments, which have an inevitable difficulty in identifying the primary species.

Until now, several groups have reported energy spectra for various elements in very high energies, extending up to a few hundreds TeV for proton and to a few tens TeV/n for heavy elements, with the use of flying vehicles such as balloon and the satellite [18–23].

While the proton spectrum obtained by different groups is in reasonable agreement, the energy spectra of other components differ with one another. Also individual data points are considerably scattered in the higher energy region, $\gtrsim$ a few hundreds GeV/n, among different groups, mainly due to poor statistics and the uncertainties in the energy calibration.

Under these circumstances, Japanese and Russian physicists started a joint collaboration, called RUNJOB (RUssia–Nippon JOint Balloon-program), on the observation of primary cosmic rays with use of the balloon-borne emulsion chamber in 1995. Two balloons were launched from Kamchatka peninsula in July 1995 for the first time, where each payload consisted of two emulsion chambers (hereafter abbreviated as EC's) with the unit size of 40×50 cm^2. We performed the same experiment further in July 1996. All EC's (eight chambers in total) were recovered successfully near the Volga region after the exposure of $\sim$150 h.

The advantage of RUNJOB is in the geographical position of each institute and the facility in ballooning, suitable for quick shipping of the payload, which is absolutely important to reduce the background in the case of the passive-type experiment. That is, the chamber is constructed in Institute of Space and Astronautical Science (ISAS) in Tokyo, and transferred to the launching site in Kamchatka via Khabarovsk, located rather near Tokyo. After recovery of the payload at the place of landing (Volga region, west side of the Ural Mountain, etc.), it is moved to Moscow via Volsk Balloon Station without delay, and photosensitive materials such as the X-ray film and the nuclear emulsion plate (hereafter abbreviated as NEP) are arranged separately from other nonsensitive materials. These films and NEP's are brought back to Tokyo by both Japanese and Russian members in the form of air-hand-luggages, and processed immediately upon the arrival at Institute of Cosmic Ray Research (ICRR), University of Tokyo.

In fact, we find NEP's used in the present experiment are surprisingly fine in spite of so long exposure as $\sim$150 h. This is because it takes only three months from the start of the nuclear emulsion pouring to the finish of the chemical

Table 1
RUNJOB campaigns in 1995 (RUNJOB I, II) and 1996 (RUNJOB III, IV)

	RUNJOB I	RUNJOB II	RUNJOB III	RUNJOB IV
Flight duration (h)	130.0	167.0	134.0	147.5
Chamber area (m^2)	0.4	0.4	0.4	0.4
Exposure ($h\,m^2$)	52.0	66.8	53.6	59.0
Chamber weight (kg)	230	230	254	254
Balloon volume (m^3)	180 000	180 000	180 000	180 000
Balloon weight (kg)	650	650	650	650
Ballast masses (kg)	800	800	800	800
Parachute weight (kg)	180	180	180	180
Contorol device weight (kg)	220	220	220	220
Total weight (kg)	2080	2080	2104	2104

processing, both of which have been carried out at ICRR.

Another reason of the cleanness of NEP is due to the cut-off rigidity of ~3 GV along the flight course in Siberian latitude [4] [24,25]. This makes us quite favourable in tracing the electron showers up to the vertex point and in identifying the kind of primary element with use of NEP on microscope, which are often buried in the background tracks, since the bulk of the background comes from those with energies less than 1 GeV. Namely, higher cut-off rigidity is more favourable for the observation of high energy cosmic-ray primaries with the use of EC.

In this paper, we summarize the results obtained by four balloon flights with eight EC's on board carried out in 1995 and 1996. In Section 2, we present the performance of the RUNJOB experiment, focusing on the flight situation, the structure of the payload, and the data processing. In Section 3, we give the energy determination applied for the RUNJOB chamber with a thin calorimeter, which is designed to reduce the weight of payload. In Section 4, we show the energy spectra for various elements obtained by the present work, and compare them with those reported by other groups in the past. Section 5 is reserved to the summary and the discussion for the present results.

[4] The polar patrol balloon provides a capability of much longer duration experiment without the sunset effect, but the cut-off rigidity goes down as small as multi-tens MV. This gives us a rather negative factor in the case of the passive-type experiment.

2. Experimental procedure

2.1. Flight performance

We have launched four balloons from Kamchatka in 1995 and 1996, and recovered all payloads successfully. The details are summarized in Table 1.

The trajectories of four balloons are shown in Fig. 1, and one finds they are impressively stable for both years. The altitude profiles of individual flights are shown in Fig. 2, where the altitude fluctuation due to the day–night effect is remarkable, and the variation between the minimum and the maximum altitudes amounts to as large as 10 g/cm^2. This variation does not bring us any serious problem for light elements such as proton and helium, since their attenuation lengths are ap-

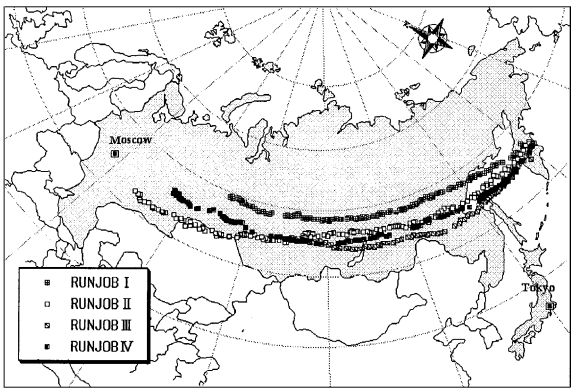

Fig. 1. Trajectories of four balloon flights performed in 1995 and 1996.

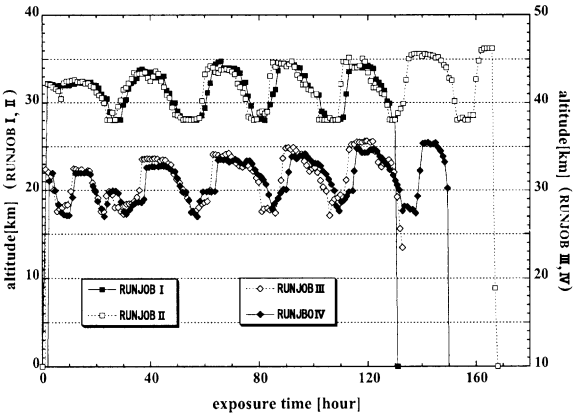

Fig. 2. Altitude profiles of four balloons.

proximately of the magnitude of 100 and 50 g/cm^2 in the atmosphere respectively.

It might become, however, effective for heavier elements, particularly for the iron with the attenuation length of $\sim$15 g/cm^2. So, we should not use a simple average altitude estimated from the flight record shown in Fig. 2, but find an effective altitude for several primary elements in order to eliminate the above uneasiness, which is discussed in detail in Appendix A.

2.2. Chamber structure

Both groups of Japan and Russia have enough experiences in EC techniques, which have following advantages in observing the high energy cosmic-ray primaries:

- the detection threshold of shower energy is rather high, $\gtrsim$ multi-TeV though slightly depends on the experimental condition, namely EC is very effective to select cosmic-ray primaries with high energies,
- EC has much larger acceptance in $S\Omega$ than that of the active-type detector,
- both analytical and the simulational studies [26–28] on the cascade shower development are well established to determine the shower energy with good accuracy.

Because the balloon performance here is limited in its volume and the weight, having 180,000 m^3 and 650 kg respectively as shown in Table 1, we cannot load EC with heavy calorimeter on board. In order to solve these difficulties, we had to design inevitably light-weight type EC by reducing the absorber thickness, whereas the energy determination using cascade shower becomes hard, particularly for high energy event, as it is discussed in the next section.

Now, we show the chamber structure of 1995 and 1996 in Fig. 3. The chamber consists of basically four parts, which provide following functions:

- primary module to identify the primary particle,
- target module to produce the interaction,
- spacer module to separate the secondary particles,
- calorimeter module to observe the electromagnetic cascade showers.

The design of large spacer enables us to measure the emission angle of both secondary particles ($\pi^{\pm}$'s, γ's) and fragments ($p, \alpha, \ldots$) coming from the break up of the heavy primaries. By using these data complementarily with the photometric data available for cascade shower energy determination, we can overcome the difficulty in the limited depth of the calorimeter with $\sim$4 radiation length in vertical, which is too thin to catch the shower maximum for very high energy events, unless the zenith angle is large enough to elongate the path length in calorimeter.

The calorimeter module is divided into two sections, upper and the lower parts. The upper calorimeter is made up of styrofoam plates (thickness of each one is 1 cm), thin lead plates (thickness of each plate is 1 mm, corresponding to 0.178 radiation length) and the sheets of photo-sensitive materials (X-ray film and NEP), which plays two roles, one to be a spacer for separating the secondaries produced in the target, and the other to help the microscopic work for tracing the electron showers from the lower calorimeter to the target.

There are some differences in the chamber structure used in 1995 and 1996 campaigns. The acrylic target plate in 1995 is replaced with the stainless steel in 1996, and the spacer thickness

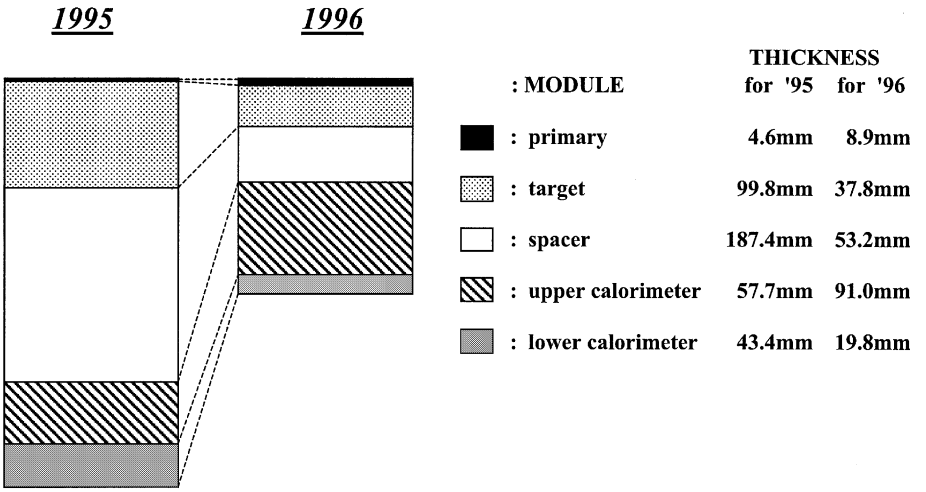

Fig. 3. Chamber structure in 1995 and 1996 experiments.

(including the upper calorimeter) in 1996 is nearly half of that in 1995. This is mainly due to an expectation to increase the efficiency in tracing work on NEP from the calorimeter layer to the target layer, namely to find the vertex point (hereafter abbreviated as VP) in target as easily as possible. These improvements indeed gave us a positive result as we have expected, while the cascade degradation effect in both target and the upper calorimeter makes us occasionally troublesome to discriminate between hadron-induced shower and γ-induced one at the early stage of the event selection in 1996 data.

One chamber has an area of 40×50 cm^2, and two chambers are put together in one box without any gap (see Fig. 21 in Appendix B). This setting condition is very effective in tracing a type of event crossing the two adjacent chambers, which increases the effective solid angle considerably in comparison with that expected from those assembled separately.

Another advantage of the present assembling scheme is that the calculation of detection efficiency becomes very simple (see Appendix B), without worrying about troublesome effects of the collision and the absorption of cosmic-ray particles in adjacent chambers.

In this experiment, we have used also a high sensitive X-ray film, called screen-type X-ray film [29,30]. The result of the analysis of this film will be reported elsewhere, which might bring us a complementary data for the present results, particularly for the iron component.

2.3. Event scanning and identification of primary particles

We start with a naked-eye scanning of the shower spots successively recorded on the multilayer stack of #200-type X-ray film in the lower calorimeter. After scanning individual dark spots on the X-ray film, their coordinates on each layer are stored on the computer hard-disk with help of the digitizer. Once we get the coordinates of individual shower spots recorded on the multilayers of X-ray film, we can easily reconstruct their trajectories by projecting each three-dimensional coordinate on a sheet of plane surface so that they are placed in a line. We call this sheet, a map.

With reference to the map, we can detect quickly the electron shower on NEP with use of the microscope. While the shower spots marked on the map are only those visible by naked eye on #200-type X-ray film, we can find very small electron showers on the NEP by referring to the map, even those invisible on the X-ray film. For

instance, a visible spot by naked-eye on X-ray film is limited to those with the net optical darkness $D_{net} \gtrsim 0.1$, where $D_{net} = D_{sp} - D_{bg}$ (D_{sp}: spot-darkness, D_{bg}: background darkness, see also Appendix B). This limitation for the visible spot-darkness on the film corresponds to approximately 50–100 electrons within the circle of 50 μm radius, though depending slightly on the experimental condition.

On the other hand, it is possible, in principle, to detect even single electron track on NEP as long as the location accuracy in shower trajectory is excellent and the background tracks are not so significant. In fact, Nishimura et al. [31] have succeeded in primary electron observation with use of the EC on board of the balloon flights performed at Sanriku Balloon Station in Japan.

Since as large as ~1 mm is the location accuracy of the map with use of the X-ray film, it is hard to trace up electron showers on NEP in the upper calorimeter and/or the target unless the shower energy is high enough with large multiplicity, say more than a few tens TeV. So, after detecting electron showers on NEP's every layer by referring to the map, all of these coordinates on NEP are stored once more on the hard-disk with help of the computer-aided-large stage (CALS), which installs the microscope and covers the movable area of 40×50 cm^2 with the accuracy of a few μm in reading the coordinates. Details are presented in Refs. [18,29,30].

To make the location accuracy of each shower more precise with use of NEP, we pick up more than 10 reference tracks of relativistic heavy primaries on NEP, penetrating from the top to the bottom in the chamber, and correct a relative setting position of each NEP on CALS so that all the reference heavy tracks are aligned simultaneously with one another. Finally, we find the location accuracy in reconstruction of the shower trajectory is ~90 μm, small enough to reach the VP with ease.

The next step is to identify the kind of primary element using upstream NEP located just above the VP, occurring mainly at acrylic plates (or stainless steel plates) in the target or at lead plates in the calorimeter. If the VP is observed luckily on NEP, the identification of the primary is of course perfect even for proton in jammed background tracks. Practically, however, most of VP are located in other nonsensitive materials such as lead and acrylic plate, and we have to search a candidate of primary track with use of the upstream NEP on microscope.

Heavy primaries ($\gtrsim$ CNO) are identified immediately without ambiguity at the first upstream NEP just above the VP, since their tracks are of heavily ionizing ones associated with δ-rays. On the other hand, in the case of helium primary, we observe sometimes a couple of candidates on NEP in the same field of vision on microscope within the circle of 90 μm radius. Then the location accuracy of 90 μm is not enough in order to identify which track is a true one among them.

To do so, we pick up at least two reference heavy tracks near the VP, usually a few centimeters distant from one another on NEP, and then confirm the true one with use of the triangulation method [32]. The location accuracy of this method is of the magnitude of 20–50 μm, depending on the relative distance between the VP and nearby reference-heavy-tracks. It is now accurate enough to identify helium tracks behind the background mainly coming from minimum ionizing tracks, as the grain density of the helium track is four times higher than that of the minimum ionizing one.

The location accuracy of 20–50 μm is still not enough for the identification of proton primary, since sometimes observed are several candidates with minimum ionizing tracks even in such a small field of vision on microscope, having the same zenith and azimuth angle as that of the electron shower of interest detected at downstream NEP's. The location accuracy must be of better than 10 μm for the *definite* identification of proton in the case of long duration experiment, while the accuracy of 100 μm is good enough in the case of short duration experiment.

In practice, we succeeded in the identification of proton some half among necessaries, where no canditates of helium and heavy tracks are observed. But, the halfness in the identification here does not matter at all, since both possibilities of helium and heavy primaries are definitely rejected

for these events, i.e., all of them must be protons (or may be neutrons produced via charge exchange process in the atmosphere), irrespective of either success or failure in the definite identification of proton. It is rather remarkable that half of proton tracks in total are identified despite of the long-duration exposure with bulky background tracks on NEP.

The location accuracy for the primary identification in the case of JACEE group is nearly the same as ours [63], while the percentage of the success in proton identification is not explicitly reported in their long duration experiments. On the other hand, Zatsepin et al. [23] reports that it is hard to discriminate between proton and helium in their long duration balloon experiments, since their location accuracy is of the magnitude over hundred micron meters. Therefore, their results on proton and helium components (see Section 4.1) are obtained only with use of short duration experiments performed at Volsk Balloon Station in Russia, where background tracks must be much reduced in comparison with those observed in the long duration experiments.

2.4. Charge determination

To avoid the laborious δ-ray counting of heavy-primary track for the charge determination, we developed a narrow-slit method using the microscope equipped with CCD camera and the monitor TV, which is auto-controllable by PC for three axes simultaneously, (x, y) on stage and z for objective lens. We briefly describe this method here, details of which are summarized in Ref. [33].

We measure the darkness of primary track within a narrow slit using CCD. The slit width must be optimized according to the kind of the primary charge. It should be narrower for lighter elements, and wider for heavier ones, otherwise the signal can be masked behind the background tracks in the former case, and the darkness is saturated in the latter case.

Also we have to eliminate the effect of the depth of focus along the track in nuclear emulsion of 60 μm thickness (100 μm in the case of those inserted in the primary module in 1995), which is taken into account by measuring automatically the darkness every 5 μm step depth by the help of z-axis controller.

Next problem is the calibration of the darkness within the narrow slit for the absolute charge determination. One might think that heavy ion beam is the most promising for this purpose. It is, however, not so simple from the practical point of view, particularly in the case of long duration balloon experiment. Since the background tracks recorded on NEP are large in this experiment, it is not useful for us to get the beam data with use of rather fresh emulsion without backgrounds. Instead, we calibrate the darkness and check the resolution of charge determination in the following way.

As presented in Ref. [18], bulky heavy-primary tracks are observed by the use of the screen-type X-ray film on board of the Sanriku balloon. The charge resolution is, for instance, 0.36 and 0.82 charge unit for oxygen and iron respectively. Among these heavy primaries, we select three typical ones, O, Si and Fe, where we pick up those within $Z \pm 0.2$ range around a Gaussian peak at Z in a charge spectrum.

Applying the present charge-determination method for those identified from Sanriku experiment, we get satisfactory results as shown in Fig. 4, where together plotted are helium results identified by counting the grain density, and several curves are drawn from the simulation calculation discussed below.

To check the resolution of charge determination, we perform extensive simulation calculations of δ-rays produced by heavy primary during the passage in nuclear emulsion, taking account of the background recorded on practical NEP on board of the RUNJOB balloon. The details of the simulation calculation are summarized in Ref. [34], and well confirmed by the comparison with heavy-ion beam data.

The simulated heavy tracks associated with jammed δ-rays are pasted randomly on RUNJOB's NEP actually exposed. We applied our charge-determination method for these artificial events, including the backgrounds observed by RUNJOB experiment, and the results are shown in Fig. 5 in the case of the path length with 200 μm.

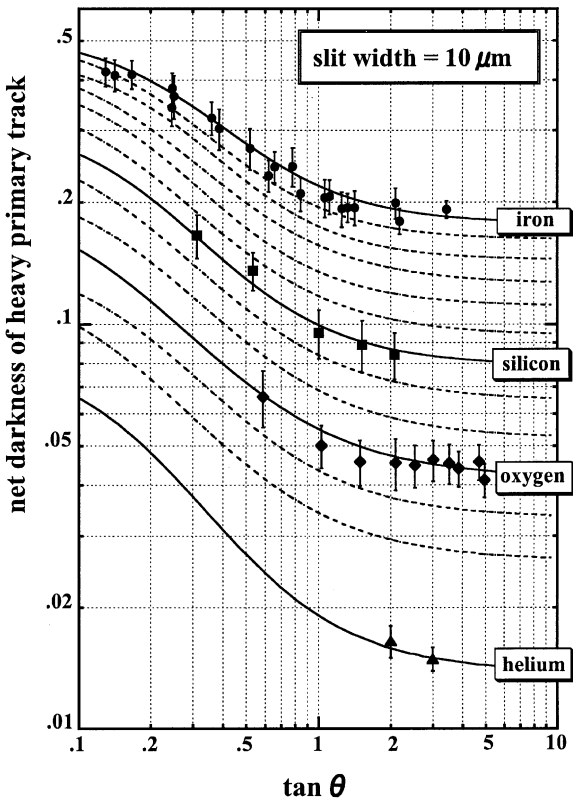

Fig. 4. Scatter plot of zenith angle vs. darkness of heavy track recorded on nuclear emulsion plate, obtained by Sanriku experiment. Curves are obtained by the simulational calculation taking the background effect into account.

Though the resolution depends naturally on the path length (practically $\gtrsim 200$ μm) used for data-taking of the track image, these results are satisfactorily enough for the practical purpose.

Table 2
Tracing results obtained by 1995 and 1996 experiments.

Primary	RUNJOB '95	RUNJOB '96
Proton	117	339
Helium	26	90
Li,Be,B	3	12
C,N,O	9	33
Ne,Mg,Si	6	11
Sub-Fe	3	4
Fe	6	2
Not identified	13	9
Total	183	500

The meaning of "not identified" appeared in the bottom line is "we could not identify the VP".

2.5. Detection efficiency

In Table 2, we summarize the statistics on tracing results, obtained by both 1995 and 1996 experiments. We meet occasionally with a difficulty in observing the VP for proton-induced interaction with small multiplicity of charged particles, mainly coming from an event of low energy interaction. Number of such type of event is also presented in the bottom line named "not identified", and the loss rate depends on chamber structure, for instance, 7% and 2% for 1995 and 1996 experiments respectively. But it does not bring us any trouble in the present result since we focus on high energy event only.

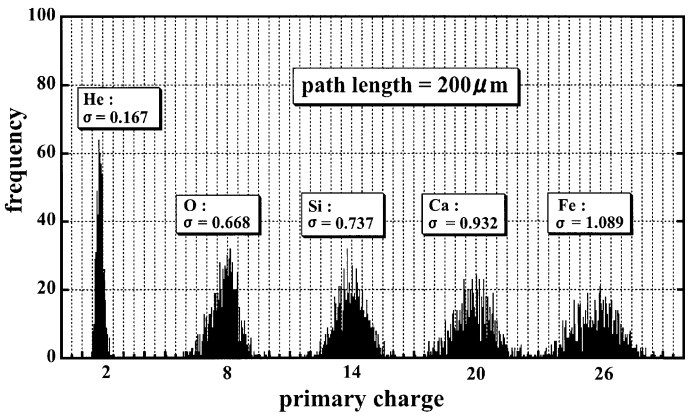

Fig. 5. Resolution of charge determination with use of narrow-slit method, taking the RUNJOB background into account.

Based on these data, we can estimate the absolute intensities for various elements as well as for all-particle by summing them.

It is needless to say that in order to evaluate them, we have to take into account the detection efficiency $\xi(E_0)$ as the function of the primary energy E_0. So, we touch upon here the detection efficiency problem in RUNJOB chamber.

This procedure is somewhat complicated, and related to various kinds of parameters, such as the chamber structure, model of the reaction cross-section, detection condition of the electron showers on X-ray film, resolution of the shower-energy determination and so on. So, we summarize the essence of the evaluation in Appendix B and show here only the numerical results from the 1995 and 1996 experiments.

In Fig. 6, we show numerical results of the detection efficiency, $\xi(E_0)$, in several cases of primary elements for the 1995 and 1996 experiments, where we calculated them by the use of the cross-section based on the soft-sphere model [57] (see Appendix B), including the dependence of projectile energy. Another choice of the cross-section is discussed in Section 5.

One finds that the detection efficiency of the 1996 chamber is much better than that of the 1995, particularly in the lower energy region. This is mainly due to two effects; i.e., one is a difference in spacer thickness and the other in dilution factor, $D_f = 1 + \Delta/L$ (L: thickness of each lead plate, and Δ: gap length between two lead plates), in lower calorimeter. Both parameters in 1996 are of the magnitude of nearly half of those in 1995 (see Section 2.2 also).

In relation to the above discussions, we have to take care also in superposing individual data of different flights in 1995 and 1996 campaigns. Naturally, one cannot superpose straightforwardly each data equally, since the effective balloon altitude, the exposure time, the chamber efficiency, etc., are all different in each flight.

To combine them, let us consider a flight j with the effective altitude t_j, the chamber area S_j, the exposure time T_j, and the detection efficiency ξ_j. Assuming the absolute differential intensity of a primary cosmic-ray as ΔI_0 at the top of the atmosphere, the observed number ΔN_j of the relevant primary is given by, (see Eq. (A.2) in Appendix A)

$$\Delta N_j = \xi_j S_j \Omega_0(\tau_j) T_j \Delta I_0 \mathrm{e}^{-\tau_j}, \tag{1}$$

where $\tau_j = t_j/\Lambda$ (Λ: attenuation length of the primary in the atmosphere), and $\Omega_0(\tau_j)$ is the effective solid angle at the altitude t_j, explicitly given by Eq. (A.3) with $k = 0$ in Appendix A.

Superposing both sides of Eq. (1) with respect to flight number j, we immediately obtain the absolute intensity

$$\Delta I_0 = \frac{\sum_j \Delta N_j}{\sum_j \xi_j S_j \Omega_0(\tau_j) T_j \mathrm{e}^{-\tau_j}}, \tag{2}$$

where we omit the parameter of energy inherent in ΔI_0, ΔN_j and ξ_j, for the sake of simplicity. The

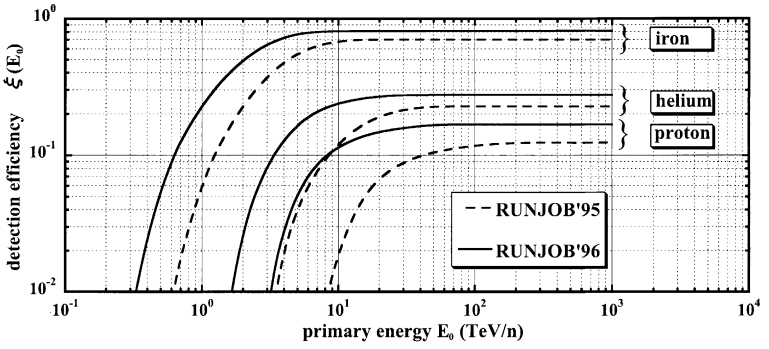

Fig. 6. Relation between detection efficiency and primary energy E_0 for 1995 and 1996 experiments.

above superposition of different flights j's must be done, of course, in each energy bin for the practical procedure.

3. Energy determination

3.1. Photometric method

Electron shower originated in a nuclear collision with materials in the chamber is easily detected by naked-eye on X-ray films inserted in the calorimeter, whereas it is visible on NEP only with help of the microscope. In addition to the validity of the naked-eye scanning of the shower spot, the development of spot-darkness successively recorded on multi-sheets of the X-ray film gives us an important information on the determination of the shower energy ΣE_γ.

The maximum darkness $D_{\max}$ in the transition curve of the shower spot-darkness is approximately proportional to ΣE_γ. The spot darkness is measured with use of the photometer, and we get immediately $D_{\max}$ by fitting a simulated transition curve onto the measured data (see Fig. 8a). Then we obtain straightforwardly ΣE_γ using the relation of $D_{\max}$ vs. ΣE_γ, taking into account various effects, such as the zenith angle effect, chamber structure, position of the VP and so on [28, 35].

Since the shower energy $\Sigma E_\gamma^{(\mathrm{photo})}$ obtained by the photometer might be affected by the amount of the background as well as the processing condition, we have to calibrate it by comparison with the energy $\Sigma E_\gamma^{(\mathrm{count})}$ obtained by the electron-counting method using NEP, which is almost free from the experimental condition.

The absolute energy calibration of our simulation calculations used for the electron-track counting was checked with use of FNAL electron-beams with 50, 100 and 300 GeV [36,37], though the electron beam with higher energies is not available nowadays. The energy calibration at higher energies $\gtrsim$ multi-TeV was performed with use of π°-peak in γ–γ invariant-mass distribution, which was obtained by Chacaltaya two-storey type EC [38,39] (see next subsection).

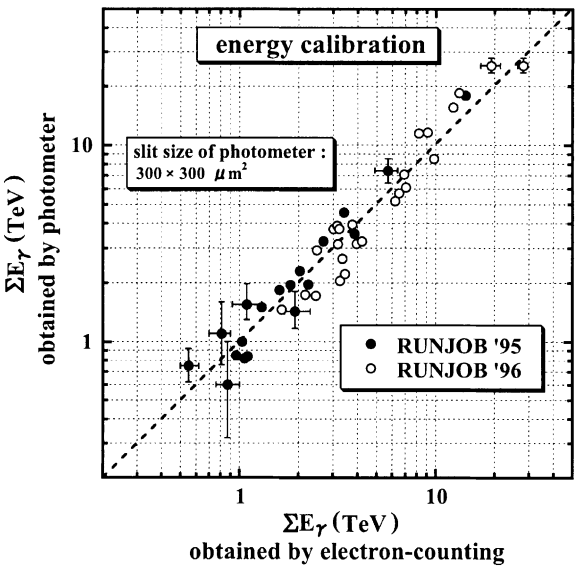

Fig. 7. Correlation between shower energies obtained by photometer method and those by electron-counting method.

In Fig. 7, we show the correlation between $\Sigma E_\gamma^{(\mathrm{photo})}$ and $\Sigma E_\gamma^{(\mathrm{count})}$ obtained by 1995 and 1996 experiments, and find no correction is necessary for the absolute value of the shower energy in both experiments. It means that the background in RUNJOB experiment is not so critical as to need the correction of the standard numerical parameters appeared in the characteristic curve of #200-type X-ray film, ρ vs. D, where ρ is the electron density and D is the optical darkness on X-ray film (see Eq. (B.9) in Appendix B).

Here, we have to recall that the calorimeter thickness of RUNJOB chamber is as thin as $\sim$4 radiation length in vertical, as mentioned in the previous section. We meet occasionally events where the shower transition curve does not reach its maximum point before leaving the bottom of the lower calorimeter, particularly in the case of very high energy events with small zenith angle. Two typical examples are shown in Fig. 8, where (a) is an example of reliable fitting, and (b) a doubtful one without observing the shower maximum. We found approximately 20% of all events are of (b)-type one. In the next subsection, we present another method to determine the shower energy for the (b)-type events.

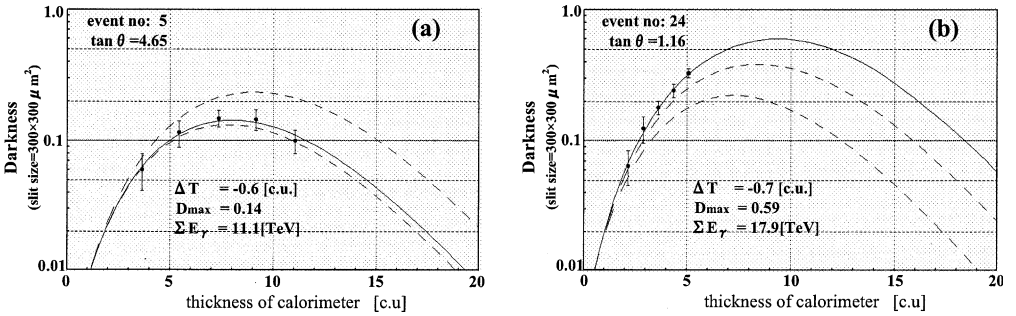

Fig. 8. Two typical examples of (a) reliable fitting and (b) doubtful one.

3.2. γ-ray core method

In RUNJOB chamber, we can measure simultaneously the emission angles of $\pi^{\pm}$, γ (via $\pi^0 \to 2\gamma$) produced by the nuclear interaction as well as those of fragment products such as proton, $\alpha, \ldots$, due to the break up of heavy primary in the case of 1995 chamber. [5] We do not discuss here the method of energy determination with use of the fragments, which is summarized in Ref. [18].

Up to now, we have proposed several methods [40–42] for the energy determination in RUNJOB chamber, using the emission angle of $\pi^{\pm}$ and γ. In this paper, we focus on a method for the determination of the shower energy ΣE_γ, transferred to γ-ray component, since the event selection is absolutely based on the shower spot recorded on X-ray film and hence the detection efficiency is closely related to the magnitude of ΣE_γ (see Appendix B).

The shower energy released into secondary γ's is immediately written down with use of the emission angle θ_i and the transverse momentum p_{ti} of each constituent γ in the following way.

$$\Sigma E_\gamma = \sum_{i=1}^{n} \frac{p_{ti}}{\theta_i} \simeq \sum_{i=1}^{n} \frac{\langle p_t \rangle(\theta_i)}{\theta_i}, \tag{3}$$

where n is the γ-ray multiplicity, and the average transverse momentum $\langle p_t \rangle$ is nearly constant with $\sim$200 MeV/c, except small emission angle in the very forward cone.

Based on the results from both cosmic-ray (Chacaltaya EC [38,39]) and the accelerator (UA7 [43]) experiments, we assume the functional form of $\langle p_t \rangle(\theta)$ is expressed as

$$\langle p_t \rangle(\theta) = p_0[1 - \mathrm{e}^{-u}], \tag{4}$$

$$u \equiv \theta \langle E_\gamma \rangle / q_0, \quad \text{and} \quad \langle E_\gamma \rangle = \Sigma E_\gamma / n, \tag{5}$$

where typical values of p_0 and q_0 are of the magnitude of 200 MeV/c and 80 MeV respectively.

Here we have to take care of a detection-threshold energy effect in applying Eq. (4) for the practical analysis. Namely, we observe only γ-cores with energies larger than some threshold energy E_c in NEP, where E_c depends on the chamber structure as well as the exposure time, for instance 50–100 GeV in the case of RUNJOB experiment and 200–300 GeV in the case of Chacaltaya experiment.

Naturally, the condition of $E_\gamma \geqslant E_c$ deforms the shape of $\langle p_t \rangle(\theta, E_c = 0)$ in Eq. (4), and we get a following relation from a simple calculation,

$$\langle p_t \rangle(\theta, E_c) \simeq \langle p_t \rangle(\theta, 0) + E_c \theta. \tag{6}$$

In Fig. 9, we show the correlation between $\theta \langle E_\gamma \rangle$ and $\langle p_t \rangle(\theta, 0)$, after eliminating the effect of E_c using Eq. (6), which is obtained by Chacaltaya two-storey-type chamber ($E_c \simeq 0.2$ TeV) and the FRITIOF simulation code [44]. The shower energies cover 3–150 TeV for the former data, and 1–200 TeV for the latter data. Curves in the figure are drawn by Eqs. (4) and (5) with two choices, $(p_0, q_0) = (200, 100)$, $(180, 60)$ in unit of (MeV/c,

[5] Unfortunately it is hard to measure the emission angle of fragments in the case of 1996 chamber, since the target material is stainless steel plate, and the discrimination between proton fragments and cascade-degraded electrons becomes difficult.

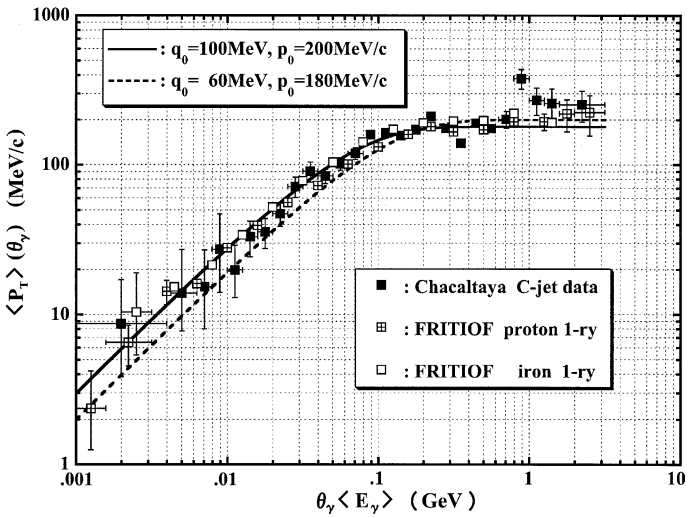

Fig. 9. Correlation between the emission angle and the average transverse momentum for γ-rays produced by nuclear interaction.

MeV). More careful fitting with Eq. (4) shows that these parameters depend weakly on ΣE_γ (see Appendix C).

It is remarkable that the Chacaltaya data (hereafter called C-jet data) agree fairly well with those expected from the simulational FRITIOF code, and also those obtained by the iron-induced jets coincide with those by the proton-induced jets. Looking at carefully Fig. 9, one might notice that the average transverse momentum, $\langle p_t \rangle$, obtained by C-jet data is slightly enhanced in large emission angle. This is fully consistent with the contribution coming from the quark-parton hard scattering [50]. The enhancement is, however, not essential for the present energy determination, but the bending region, $\theta_\gamma \langle E_\gamma \rangle \sim 0.1$ GeV, is the most important.

Now, we consider the physical meaning of the average energy $\langle E_\gamma \rangle$ appeared in Eq. (5). Since the threshold energy E_c of each constituent γ detected in NEP is 50–100 GeV in the case of RUNJOB experiment, the energy sum of γs, ΣE_γ, is naturally less than the true one released over the whole phase space, $\theta^* = 0$–π in CMS. As presented later in more detail, the former energy is 11% less than the latter, based on the simulation calculation.

From the view point of fireball picture, one might remark that γs mentioned here are those produced by the decay of the fastest moving cluster only, neglecting the second and subsequent ones.

In order to select γs belonging to the fastest cluster, we pick up only those satisfying a condition

$$\eta > \eta_{\max} - \Delta\eta, \quad \text{with } \Delta\eta = 3, \tag{7}$$

where η is a familiar variable, pseudo-rapidity ($= -\ln \tan \theta/2$), and $\eta_{\max}$ is the highest pseudo-rapidity. Therefore, the multiplicity n of γs in Eqs. (3)–(5) is not always equal to the observed one. The selection condition with $\Delta\eta = 3$ in Eq. (7) corresponds to the collection of approximately 90% of γs produced by the isotropical decay of the fireball.

For the practical procedure in grouping γs defined by Eq. (7), we use the second highest pseudo-rapidity, $\eta_{\max 2}$, instead of $\eta_{\max}$ in order to avoid a fluctuation in the emission angle of top γ, while the simultaneous determination of the shower energy and the energy-weighted center (see later discussion in this subsection) is performed with inclusion of the top γ.

Now, we can regard the group of γs selected by Eq. (7) as "effective" one in the total shower energy released over the whole space in CMS, in the sense that most of the shower energy is transferred

into this group in the laboratory system. So, all physical quantities, such as ΣE_γ, n and $\langle E_\gamma \rangle$, are used tacitly in the meaning of effective ones in the following discussion.

Let us present explicitly how to get the shower energy ΣE_γ from the γ-core data. To make the procedure simple, we omit here the effect of the threshold energy E_c in detecting each core, whereas the exact procedure is summarized in Appendix C, taking its effect into account.

From Eqs. (3) and (4), we find immediately a transcendental equation with respect to $\langle E_\gamma \rangle$ inherent in u_i

$$\frac{1}{n}\sum_{i=1}^{n} f(u_i) = 1, \tag{8a}$$

where we defined a function

$$f(u) = \frac{p_0}{q_0}\,\frac{1-\mathrm{e}^{-u}}{u}. \tag{8b}$$

We can solve easily the above equation with respect to $\langle E_\gamma \rangle$ by use of the iteration method, and then we obtain the shower energy ΣE_γ $(= n\langle E_\gamma \rangle)$. But there exists a critical problem in the application for RUNJOB data in practice. Namely, we can observe only the coordinate of each γ-core [6] on the target diagram, $\mathbf{r}_i(x_i, y_i)$, and the height h from the plane of the target diagram to the VP in the raw data, while the energy-weighted centre, $\mathbf{r}_G(x_G, y_G)$, is not available. It may seem to be troublesome in estimating the emission angle θ_i $(= |\mathbf{r}_i - \mathbf{r}_G|/h)$ of each γ-ray, but this problem is easily solved in the following way.

The energy-weighted centre is given by

$$\mathbf{r}_G = \sum_{i=1}^{n} E_{\gamma i}\mathbf{r}_i \Big/ \sum_{i=1}^{n} E_{\gamma i}, \tag{9}$$

and using a relation $E_{\gamma i} = p_{ti}/\theta_i \simeq \langle p_t \rangle(\theta_i)/\theta_i$, we finally get following equations from Eqs. (4) and (9),

$$\langle f(u) \rangle_n = 1, \tag{10a}$$

$$\langle x f(u) \rangle_n = x_G, \tag{10b}$$

$$\langle y f(u) \rangle_n = y_G, \tag{10c}$$

where the meaning of $\langle \cdots \rangle_n$ is

$$\langle X \rangle_n = \frac{1}{n}\sum_{i=1}^{n} X_i, \tag{11}$$

and

$$u_i = \frac{\sqrt{(x_i - x_G)^2 + (y_i - y_G)^2}}{h}\,\frac{\langle E_\gamma \rangle}{q_0}. \tag{12}$$

We have to solve the above equations simultaneously with respect to $(\langle E_\gamma \rangle;\ x_G, y_G)$, and then get the shower energy $\Sigma E_\gamma = n\langle E_\gamma \rangle$. The solution is obtained with use of the iteration method (see Appendix C).

Now let us check the reliability of the present energy-determination method by applying it for Chacaltaya experimental data and FRITIOF simulation ones. The structure of Chacaltaya two-storey-type chamber is basically the same as RUNJOB chamber, but the spacer of the former is $\sim$170 cm, that is much longer than the latter with $\sim$20 cm. Therefore, in Chacaltaya chamber, it is possible to estimate the energy of individual γ-core's by counting the electron number without worrying about the mixture of each core as in the case of RUNJOB chamber, and get the shower energy ΣE_γ by summing up the individual γ-ray energies.

In addition to the information on the energy $E_{\gamma i}$ of each constituent γ-core as well as its coordinate (x_i, y_i), the advantage of C-jet data is in the range of the detected shower energy ΣE_γ that covers 3 $\sim$150 TeV, just the region of interest in RUNJOB experiment.

Energy resolution, $\Delta E_\gamma/E_\gamma$, is $\sim$15% for each γ-ray in C-jet data, which is confirmed from the π^0-peak in the invariant mass distribution of γ–γ [38,39], so that it is quite interesting and important to compare the energies obtained by the present energy determination with those given by C-jet data.

[6] In principle, we can determine also the energy of individual γs by counting electron number with use of NEP. But it is quite hard to count the electron number separately from those originated in another γ-core, because they are often overlapped, particularly in the central region, due to the limited spacer with 20–30 cm size in RUNJOB chamber.

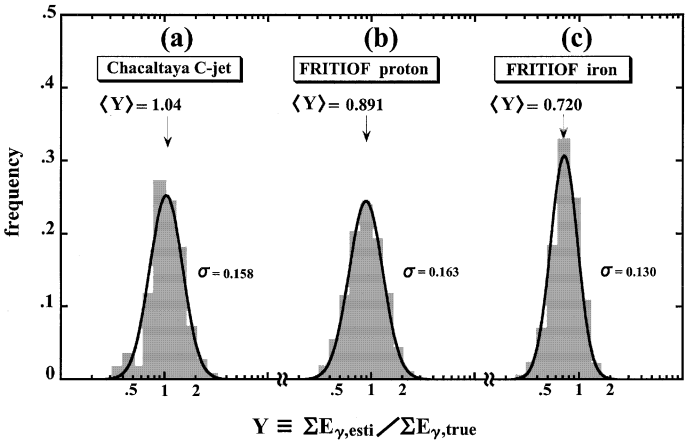

Fig. 10. Histograms of $\log_{10}[\Sigma E_{\gamma,\mathrm{esti}}/\Sigma E_{\gamma,\mathrm{true}}]$ for three data, (a) C-jet data, (b) FRITIOF code for proton primary, and (c) FRITIOF code for iron primary. Primary particle of C-jet data is of nucleon (or charged pion). The subscripts "esti" and "true" denote the estimated shower-energy and the true one respectively.

In Fig. 10a, we show a histogram of the ratio, $Y \equiv \log_{10}[\Sigma E_{\gamma,\mathrm{esti}}/\Sigma E_{\gamma,\mathrm{true}}]$, where $\Sigma E_{\gamma,\mathrm{esti}}$ is the shower energy estimated by the present method taking into account the threshold energy effect ($E_c = 0.2$ TeV), and $\Sigma E_{\gamma,\mathrm{true}}$ is the true one obtained by C-jet data. By fitting a Gaussian curve onto the histogram, we find $\sigma = 0.158$ around $\langle Y\rangle = 1.04$, that is satisfactory enough for the present purpose.

Fig. 10b is the same histogram as shown in Fig. 10a, but obtained with use of the FRITIOF code, where $\Sigma E_{\gamma,\mathrm{true}}$ means the shower energy including γs radiated backward in CMS, whereas $\Sigma E_{\gamma,\mathrm{esti}}$ is an "effective" one as mentioned before. Therefore, the peak position $\langle Y\rangle$ is shifted to 11% less than unity, and we have to correct this effect for the practical energy determination, while no shift is necessary in Fig. 10a, because $\Sigma E_{\gamma,\mathrm{true}}$ in C-jet data is also the effective energy transferred by the fastest moving cluster only.

The present method is applicable also for the heavy particle initiated shower, and we use here the FRITIOF code in order to make artificial target diagrams of γ-cores. The result is demonstrated in Fig. 10c for iron primary, in the same form as Fig. 10a and b, where the Gaussian curve with $\sigma = 0.130$ is drawn together. The dispersion is much smaller than those found in the proton-initiated shower. This is due to the fact that the multiplicity of γ-ray's produced by heavy-primary interaction is considerably larger than that in the case of proton.

We note again that the peak position $\langle Y\rangle$ is shifted to 28% less than unity due to γs radiated backward in CMS, which is of course taken into account in the practical procedure in estimating the shower energy ΣE_γ. We call the inverse of $\langle Y\rangle$ as the scale-shift factor S_{shift}, which is given in Table 6 in Appendix C for proton, helium and iron primaries.

In Fig. 11, we show a scatter plot of $\Sigma E_\gamma^{(\mathrm{photo})}$ vs. $\Sigma E_\gamma^{(\mathrm{core})}$ obtained by RUNJOB data for several primary elements, where the former energy is determined by the photometeric method described in Section 3.1, and the latter by the present γ-core method. One finds they distribute along the straight line of 45° with the dispersion of ~0.15, well within the allowable fluctuation.

Now, once we confirmed that the shower energy ΣE_γ is determined with good accuracy even in the case of the thin-type calorimeter, the final procedure is to convert ΣE_γ into the primary energy E_0. The conversion of ΣE_γ into E_0 is, however, not so simple, and must be checked carefully with use of various kinds of simulation codes, which relates also to the detection efficiency problem.

So, we discuss this problem in detail in Appendix D, and give here only the numerical results

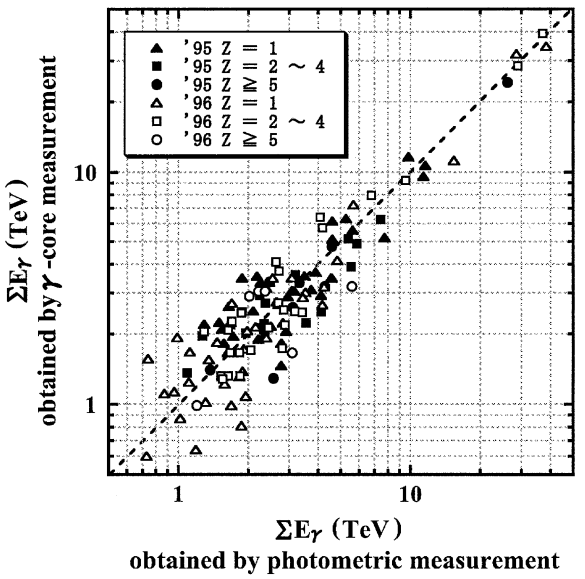

Fig. 11. Scatter plot of the shower energies obtained by photometric method vs. γ-core method.

of the conversion factor C_γ $(= E_0/\Sigma E_\gamma)$ in Table 3 used in the present work. These results agree with the past works [23,45,63] (see Appendix D), taking the different chamber structure into account.

One may remark in Table 3 that the difference between two conversion factors is rather small, one originated in the target jet (T-jet) and the other in the calorimeter jet (Cal.-jet), whereas the original average inelasticity per interaction, $\langle k_\gamma \rangle$, is quite different between light and heavy targets, particularly in the case of heavy projectile, as shown in Table 8 in Appendix D. This is because the effect of successive interactions become significant in the case of T-jet, while it is negligible in the case of Cal.-jet.

4. Experimental results

4.1. Proton and helium components

We show proton and helium spectra in Fig. 12 together with those obtained by other groups [19–21,23,46,64], where the vertical axis is multiplied by $E_0^{2.5}$. The error-bar appeared in the present work is evaluated on the basis of the Poissonian distribution instead of the Gaussian one, given by $\pm\sqrt{N}$ in the case of N counts. This is because the latter approach is acceptable only if N is reasonably large, whereas the statistics of higher energy events is small in general in the cosmic-ray experiments [47].

Now, we have no indication of the bending in the proton spectrum up to more than 100 TeV, and in opposite, find an existence of PeV-proton (see next subsection), which is far from the cut-off at around 100 TeV expected from the current model.

Our proton spectrum is in good agreement with other data within statistical errors. On the other hand, the absolute intensity of our helium spectrum is of approximately factor two lower than those obtained by JACEE [19,20] and SOKOL [21], while our data agrees rather well with those obtained by MUBEE [23] and Grigorov et al. [64].

In Fig. 13, we plot our proton and helium spectra together with the counter experiments covering lower energy region [46,48] in the form of the intensity vs. the primary energy per nucleon. Fitting a following power-like spectrum onto our data with use of the method of least squares,

$$\frac{\mathrm{d}I}{\mathrm{d}E_0} = I_0 E_0^{-\beta},$$

Table 3
Conversion factor C_γ for various elements based on FRITIOF code

	Proton ($\beta = 2.8$)	Helium ($\beta = 2.8$)	C, N, O ($\beta = 2.7$)	Ne, Mg, Si ($\beta = 2.7$)	Iron ($\beta = 2.6$)
1995 T-jet	3.65	6.01	9.35	11.3	15.2
1995 Cal.-jet	3.70	5.50	7.80	9.10	11.6
1996 T-jet	3.62	5.62	8.32	9.90	13.0
1996 Cal.-jet	3.64	5.30	7.45	8.63	10.9

T-jet means the target jet occurred at acrylic plate for 1995 chamber and/or at stainless steel plate for 1996, and Cal.-jet means the calorimeter jet occurred at lead plate. β is the exponent of differential energy spectrum.

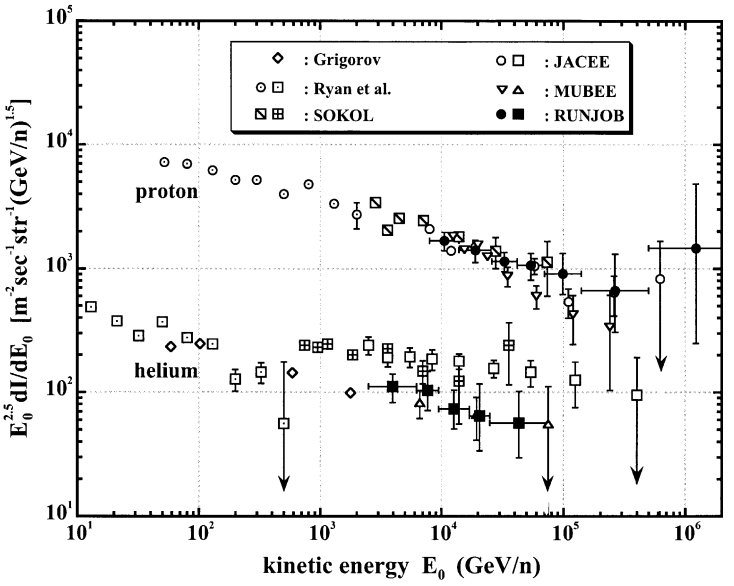

Fig. 12. Proton and helium spectra obtained by different groups. The vertical axis is multiplied by $E_0^{2.5}$ in order to emphasize the spectral feature.

we obtain

$$\beta_{\mathrm{p}} = 2.78 \pm 0.05, \qquad \beta_{\alpha} = 2.81 \pm 0.06, \tag{13}$$

and

$$I_{\mathrm{p},0} = (2.26 \pm 0.13) \times 10^4, \tag{14a}$$

$$I_{\alpha,0} = (1.50 \pm 0.11) \times 10^3, \tag{14b}$$

where suffixes p and α denote proton and helium respectively, and I_0 is given in unit of (m^2 s str (GeV/n))$^{-1}$. We draw these lines together with experimental data in Fig. 13, and find that the counter data are well on these extrapolated to the lower energy region.

Although our data do not show any difference in spectral shape between proton and the helium components at least up to 50 TeV/n, this problem is very interesting in connection with a non-linear shock acceleration process in SNR's proposed by Ellison [49], predicting subtle differences in the power index between these two, because ions with larger mass to charge ratio are accelerated more efficiently.

In this stage, we cannot say definitely whether the spectra of two elements are parallel or not in the higher energy region, and we reserve the conclusion until the completion of full data analysis of RUNJOB experiments, including most recent flights performed in 1999.

4.2. PeV-proton event

Among proton-induced interactions observed in 1995 experiment, we detected an event with the shower energy ΣE_γ more than 500 TeV. The interaction takes place in the top lead plate in the lower calorimeter, and the primary proton is fortunately identified at the NEP inserted just above the top lead plate. In Fig. 14, we illustrate the picture of this event.

As discussed in Section 2.2, the thickness of our calorimeter is not enough to catch the shower maximum in the transition of spot darkness for very high energy event, unless the zenith angle of incident shower is large enough to elongate the path length in the calorimeter.

In Fig. 15, we demonstrate the transition curve of this event, where one finds the observed spot

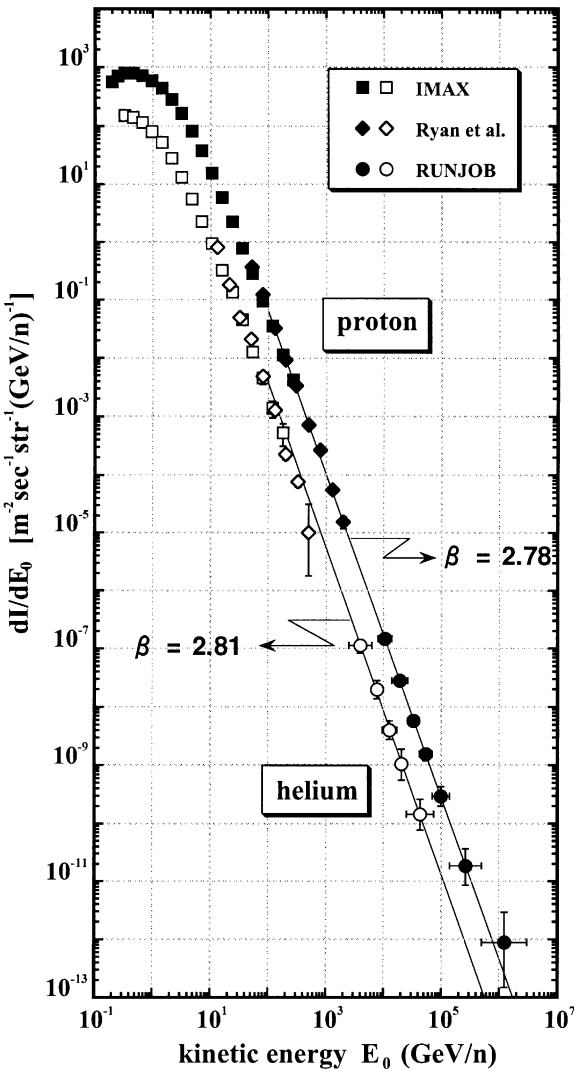

Fig. 13. Comparison of our proton- and helium-spectra with those covering the lower energy region presented by the other groups.

darkness doesn't reach a shower maximum as expected. So, it seems very hard to estimate ΣE_γ in an ordinary way.

Fortunately, however, there were two sheets of #200-type X-ray films in the barrier envelope inserted at the bottom of the chamber box as shown in Fig. 14, which were prepared for the purpose of test processing.

The electron shower developed in the calorimeter module spreads geometrically into downstream layers without suffering the cascade process after leaving the bottom lead plate in the chamber. Then we expect to get some information on the shower energy by comparing the spot darkness recorded on two X-ray films, one just beneath the bottom lead plate (named the film A) and the other in the barrier envelop (named the film B), with relative distance of $\sim$4 cm taking the inclination effect into account.

We measured the spot darkness D_A and D_B recorded on two X-ray films, A and B respectively, with use of the photometer for several sizes of diaphragm slit. We show the ratio D_A/D_B for several slit sizes in Fig. 16. We performed also simulation calculation [35] to obtain the ratio D_A/D_B, taking into account the exact configuration of the chamber structure, where the cascade process even in the light materials (X-ray film, NEP and wood base) other than lead plate is also included. Numerical curves are drawn together with experimental data in Fig. 16, which are well within two simulational curves of 500 and 1000 TeV in ΣE_γ.

While it is very hard to convert ΣE_γ into the primary energy E_0 on event by event basis, the conversion factor is supposed to be 3–5 on average from Table 3, corresponding to 0.20–0.33 in effective value of k_γ, which is consistent with various past considerations by many authors [38,39,45, 50,51]. So, the primary energy of this event can be of the order of magnitude of at least multi-PeV.

It is, however, important here to emphasize an evidence that there exists multi-PeV proton, indicating the absence of cut-off region somewhere around 100 TeV, in contradiction to what is expected by the current model, no matter if the energy of the present event might be 2 or 5 PeV.

The present method tells us at the same time that it is possible to determine the shower energy with $\gtrsim$ 100 TeV even in the case of thin-type EC, if we have an additional information on the lateral spread of the electron shower after leaving the calorimeter. In fact, taking the advantage of the present result more positively, we designed a new module, called "diffuser", beneath the calorimeter in recent RUNJOB chambers performed in 1997 and 1999, which consists of several layers of photo-sensitive materials (X-ray film and NEP) and the spacers alone, without any other heavy mate-

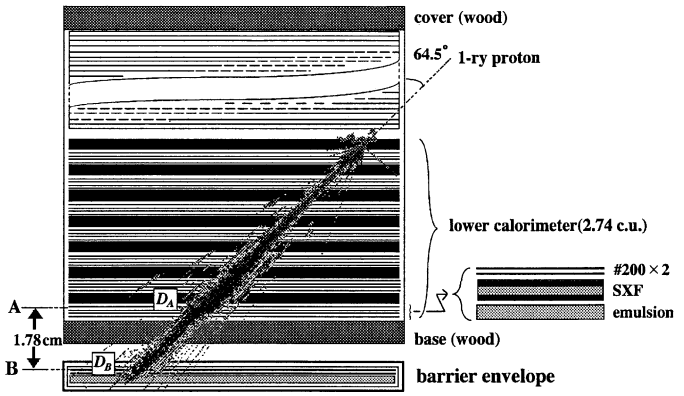

Fig. 14. Illustration of a PeV-proton event detected in 1995 chamber.

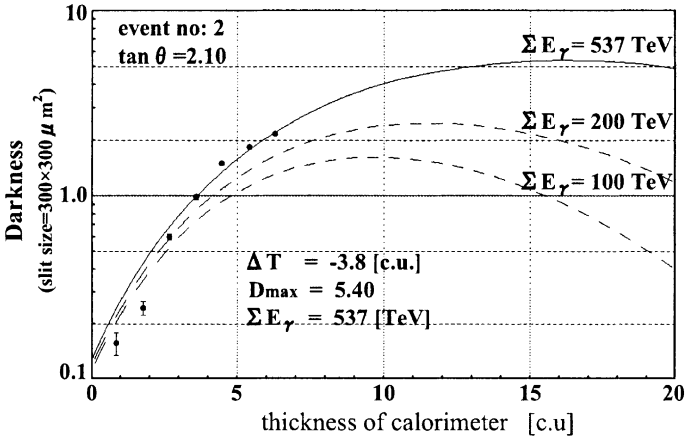

Fig. 15. Transition curve of the spot darkness obtained by the photometric measurement with the slit size of 300×300 μm^2 for the PeV-proton event recorded on #200-type X-ray film.

rials. We will report these results in the near future.

4.3. Heavy components

Though the statistics is not enough, we demonstrate the present results in Fig. 17, together with those obtained by other authors [19–22], where three typical groups, CNO-group, NeMgSi-group and Fe-group ($Z = 26$–28), are summarized. [7] We have to note that the JACCE [19,20] and SOKOL [21] data include sub-iron elements ($Z = 17$–25) in Fe-group.

Our fluxes of these three heavy components are in good agreement with other two groups, JACEE and SOKOL, in the energy region less than 10 TeV/n. Looking at carefully Fig. 17, however, our spectra on CNO and NeMgSi decrease monotonically with higher energy, while those of the other two groups show rather enhancement in the higher energy region $\gtrsim 10$ TeV/n, particularly for CNO elements.

If we focus on the data presented only by RUNJOB and Chicago group [22], all elements seem to decrease monotonically, and the slope of

[7] In the past preliminary reports on RUNJOB results [65,66], we have demonstrated 20–30% lower intensities than those shown in Fig. 17. This is due to a revised calculation for the conversion factor and the detection efficiency.

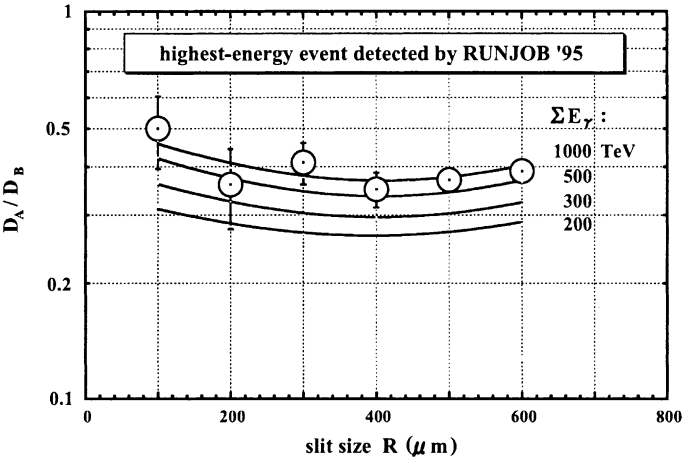

Fig. 16. Attenuation rate of spot darkness between two positions, A and B (see Fig. 14), obtained by the photometeric measurement with six slit sizes. Four curves are drawn by full simulational calculations, taking into account the exact chamber structure.

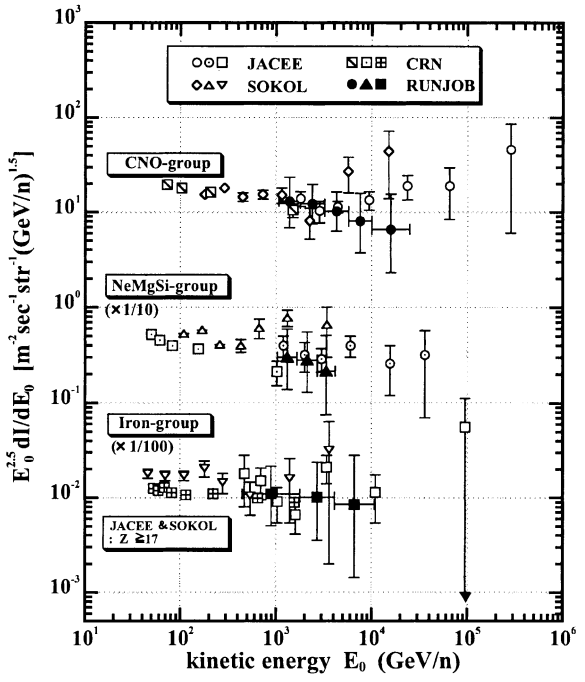

Fig. 17. Heavy component spectra obtained by different groups.

the spectrum becomes gradually harder as the mass gets heavier, for instance, ~2.70 for CNO-group and ~2.55 for Fe-group.

4.4. All-particle spectrum

Summing up the spectra for individual elements presented in Sections 4.1 and 4.3, we can get the all-particle spectrum. In Fig. 18, we show it together with data obtained by other groups [19,21, 52], where the grey zone [18] denotes the summation of individual fluxes obtained by the past direct measurements with the use of counter devices.

While all the data are well consistent with one another in the energy region $\lesssim 100$ TeV/particle, our all-particle intensity is approximately 30% less than those obtained by others in the higher energy region $\gtrsim 100$ TeV/particle, though the statistics are poor.

Fitting a following straight line onto our data,

$$\frac{\mathrm{d}J}{\mathrm{d}E_{\mathrm{P}}} = J_0 E_{\mathrm{P}}^{-\beta},$$

we find

$$\beta = 2.78 \pm 0.07, \tag{15}$$

$$J_0 = (6.92 \pm 0.56) \times 10^4, \tag{16}$$

in unit of $(\mathrm{m}^2\,\mathrm{s}\,\mathrm{str}\,(\mathrm{GeV/particle}))^{-1}$. The extrapolation of this line to the lower energy region seems

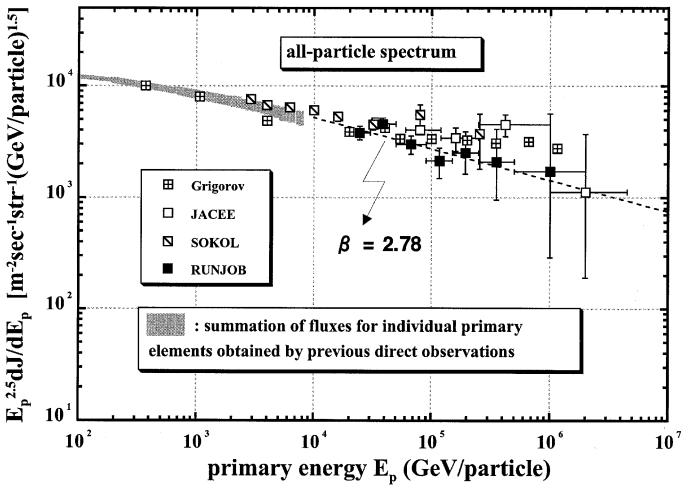

Fig. 18. All-particle spectrum obtained by different groups. Grey zone corresponds to the estimation from the summation of individual elements reported by the past direct experiments.

to be consistent with the grey zone obtained by the past direct experiments as shown in Fig. 18.

The slope obtained here is distinctively harder than the spectrum index of ~3.1 nowadays confirmed by air shower experiments beyond the knee, although the *absolute* intensity still fluctuates considerably among individual air shower groups [53].

Now, the problem is how these two slopes, below and the above the knee, can be linked to each other. There are three possibilities; first is an existence of "bump" somewhere around PeV region, the second is "flattering" before dropping, and the third is "smooth dropping". According to recent air shower experiments, the first possibility seems to be ruled out [53,54], but the other two possibilities are difficult to evaluate at this stage from both direct and indirect observations. These problems are very important for the study of cosmic-ray origin and the acceleration mechanism [55].

4.5. Average mass

It is decisively important for the understanding of the origin and the acceleration mechanism of high energy cosmic-rays to reveal experimentally the chemical composition, particularly around the knee region. Unfortunately, however, it is hard to observe separately each element with enough statistics in such high energy region. So, instead we estimate the average mass number expressed as

$$\langle \ln A \rangle (E_{\mathrm{P}}) = \frac{\sum_{\ell} \Delta J_{\ell} \ln A_{\ell}}{\sum_{\ell} \Delta J_{\ell}}, \tag{17}$$

where E_{P} is a primary energy per particle, and ΔJ_{ℓ} is a differential intensity in the energy bin $(E_{\mathrm{P}}, E_{\mathrm{P}} + \Delta E_{\mathrm{P}})$ for the element ℓ with mass number A_{ℓ}.

In Fig. 19, we show the present result together with JACEE data [19,20], where the grey zone [18] corresponds to the average mass number estimated from the past direct-observations with use of the counter devices. One finds the average mass number is of the magnitude of 4–6 (He–Li) around 10 TeV/particle.

It is remarkable that JACEE and our data are in nice agreement with each other in the energy region $\lesssim 100$ TeV/particle. JACEE data show, however, a gradual increase in mass number at higher energies, while our data seem to be almost constant over the wide energy range, 20–1000 TeV/particle.

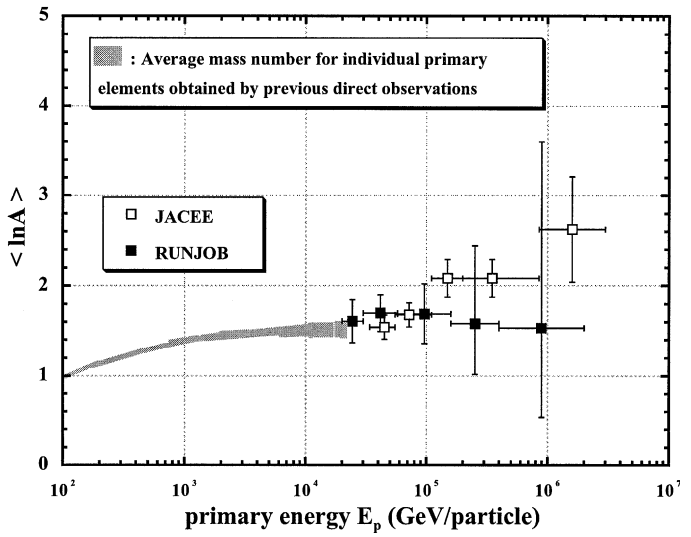

Fig. 19. Energy dependence of average mass number of primary cosmic-ray particles. Grey zone is estimated from the past direct measurements on the intensities for individual elements.

Unfortunately, the statistics of our data is very poor in the higher energy region and it should be reserved for the full analysis in the future to conclude whether the mass increases significantly with the energy beyond hundred TeV.

5. Summary and discussion

Based on eight EC's exposed on board of the long-duration RUNJOB-balloon flights performed in 1995 and 1996, we present the experimental results on the composition and the energy spectra of the cosmic-ray primaries. Numerical values of differential intensities for individual elements as well as the all particle are explicitly summarized in Table 4.

Here we summarize the essence of our results presented in the last section as following:

- our proton spectrum covers 10–500 TeV, and is nearly consistent with those reported by other groups in the past,
- a proton with multi-PeV energy is observed, and the estimated flux of this event coincides with a simple extrapolation from the above energy range with the power index 2.8,
- our helium spectrum covers 3–70 TeV/n, and its intensity is nearly half of the value obtained by JACEE and SOKOL, but in good agreement with that by MUBEE and Grigorov et al.,
- our proton and helium spectra are nearly parallel with a common index of $\sim$2.8, both consistent with the extrapolation of data obtained by the past counter experiments in the lower energy region, $\lesssim$ multi-TeV/n,
- the present absolute fluxes of both CNO-group and NeMgSi-group are in good agreement with other groups in the energy region $\lesssim$ 10 TeV/n,
- but our spectrum of CNO does not increase so significantly with higher energies as JACEE and SOKOL indicate,
- Fe-spectrum is in agreement with those given by other groups within statistical errors,
- our spectra on heavy components, CNO-group, NeMgSi-group and Fe-group, lie on the extrapolation from Chicago data,
- the slope of the energy spectra of heavy components seems to become gradually harder with increasing mass number, i.e., $\sim$2.70 for CNO-group and $\sim$2.55 for Fe-group, if we are based only on Chicago data and our data,

Table 4
Numerical table of absolute differential intensities for individual elements and all-particle

Primary	Energy range (GeV/particle)	Absolute flux ($m^{-2}\,s^{-1}\,str^{-1}$ $(GeV/particle)^{-1}$)
Proton	0.80–1.40 (4)	$1.46\,^{+0.25}_{-0.25}\,(-7)$
	1.40–2.60 (4)	$2.80\,^{+0.57}_{-0.57}\,(-8)$
	2.60–4.20 (4)	$5.77\,^{+1.02}_{-1.02}\,(-9)$
	4.20–7.00 (4)	$1.56\,^{+0.38}_{-0.38}\,(-9)$
	0.70–1.40 (5)	$2.95\,^{+1.35}_{-0.95}\,(-10)$
	1.40–5.00 (5)	$1.84\,^{+1.78}_{-1.00}\,(-11)$
	0.50–3.00 (6)	$8.80\,^{+20.2}_{-7.31}\,(-13)$
Helium	2.50–6.25 (3)	$1.13\,^{+0.29}_{-0.29}\,(-7)$
	6.25–9.50 (3)	$1.98\,^{+0.83}_{-0.62}\,(-8)$
	0.95–1.70 (4)	$4.04\,^{+1.70}_{-1.25}\,(-9)$
	1.70–2.50 (4)	$1.06\,^{+0.85}_{-0.50}\,(-9)$
	2.50–7.50 (5)	$1.45\,^{+1.16}_{-0.69}\,(-10)$
C, N, O	1.07–1.79 (3)	$1.83\,^{+1.47}_{-0.87}\,(-7)$
	1.79–3.21 (3)	$4.38\,^{+2.63}_{-1.68}\,(-8)$
	3.21–5.71 (3)	$8.49\,^{+5.10}_{-3.26}\,(-9)$
	0.57–1.00 (4)	$1.62\,^{+1.57}_{-0.88}\,(-9)$
	1.00–2.50 (4)	$2.10\,^{+2.84}_{-1.37}\,(-10)$
Ne, Mg, si	1.04–1.67 (3)	$4.76\,^{+4.60}_{-2.57}\,(-8)$
	1.67–2.71 (3)	$1.35\,^{+1.31}_{-0.73}\,(-8)$
	2.71–4.17 (3)	$3.29\,^{+4.44}_{-2.14}\,(-9)$
Iron	0.45–1.79 (3)	$4.58\,^{+4.43}_{-2.48}\,(-8)$
	1.79–4.11 (3)	$2.65\,^{+3.58}_{-1.72}\,(-9)$
	0.41–1.07 (4)	$2.36\,^{+5.44}_{-1.96}\,(-10)$
All particle	2.00–3.00 (4)	$4.04\,^{+0.57}_{-0.57}\,(-8)$
	3.00–5.00 (4)	$1.54\,^{+0.20}_{-0.20}\,(-8)$
	5.00–9.00 (4)	$2.57\,^{+0.49}_{-0.49}\,(-9)$
	0.90–1.50 (5)	$4.62\,^{+1.39}_{-1.39}\,(-10)$
	1.50–2.50 (5)	$1.53\,^{+0.83}_{-0.54}\,(-10)$
	2.50–5.00 (5)	$2.80\,^{+2.71}_{-1.51}\,(-11)$
	0.50–2.00 (6)	$1.71\,^{+3.93}_{-1.42}\,(-12)$

The meaning of $(\pm n)$ is to multiply numerical values in the column of the energy range and/or the absolute flux by $10^{\pm n}$.

- all-particle spectrum is quite consistent with those given by other groups in the past in the energy region $\lesssim 100$ TeV/particle,
- but the present intensity is $\sim$30% less than those in the higher energy region beyond 100 TeV/particle,
- the average mass is nearly constant over the wide energy range 20–1000 TeV/particle.

In the above several items, one must be concerned about the facts that our intensity of the helium and those of MUBEE and Grigorov et al. are nearly half of those obtained by JACEE and SOKOL.

Our results presented in the last section are based on the soft-sphere model [57] to get the detection efficiency, so that another choice of the model for the reaction cross-section might boost considerably the intensities of the helium and heavier components. In fact, JACEE group [63] has used the hard-sphere model [56], but as discussed in Appendix B, our cross-section is at most 10–20% higher than that expected from the hard-sphere model, a typical opposite one to the soft-sphere model. Namely, even if we use an alternative model for the calculation of the detection efficiency, our intensities shown in the last section

increase only 10–20%, which cannot at all explain the difference between our data and those by the other two groups.

While our data is not yet full and do not include the most recent experimental data, we believe these discrepancies are not simply due to a statistical reason, but could be caused by some methodological problems, such as the energy calibration, [8] the detection efficiency calculation, the primary identification, etc. So, we reserve the discrepancies mentioned here for further studies in the future, taking the above possibilities into account.

Present results are based on 40% of data obtained in RUNJOB experiments, and the results of complete analysis will be reported in the near future.

Acknowledgements

This work is supported by Institute of Cosmic Ray Research (ICRR), University of Tokyo, Institute of Space and Astronautical Sciences (ISAS), Japan Society of Promotion of Sciences (JSPS), Grants-in-Aid for Scientific Research and also for International Science Research from the Ministry of Education, Science, Sports and Culture in Japan (grant no. 08404012, 08045019 and 111695026), and Russian Foundation of Fundamental Research (grant no. 00-15-96632), International Projects of Russian Ministry of Science and Technology, and Russian Commission on Balloon Research, Grants PFFI 99-02-1772, 99-02-31005, 99-02-18173, Grant "Universiteti Rossii" 990592 in Russia.

We particularly acknowledge all staffs of the emulsion division of ICRR, the balloon division of ISAS, Volsk Expeditionary Base and Moscow State University for their helpful works at various levels to realize RUNJOB-program.

[8] The transition curves used for the determination of the cascade shower energy in JACEE are the same as those used in RUNJOB, both groups basing a common Ref. [35]. So, the difference between RUNJOB and JACEE cannot be due to the energy calibration.

Appendix A. Effective altitude of the balloon and the atmospheric correction

As shown in Fig. 2, the altitude fluctuation of RUNJOB balloon is rather significant, so that we show here how to estimate the effective altitude for such fluctuation.

Vertical intensity of the cosmic-ray particle $I_\perp$ at an observational level of t g/cm^2 is given by

$$I_\perp(\tau) = I_0 \mathrm{e}^{-\tau}, \quad \text{with } \tau = t/\Lambda, \tag{A.1}$$

where I_0 is the absolute intensity of the particle at the top of atmosphere, and Λ is its attenuation length.

Now, the number of particles N_{obs} incident upon the chamber with area S for the exposure time T at the altitude t is immediately written down, taking the zenith-angle effect into account, as

$$\begin{aligned} N_{\mathrm{obs}} &= ST \int\int_{\Omega \leqslant 2\pi} \cos\theta I_\perp(\tau/\cos\theta)\,\mathrm{d}\Omega \\ &= [S\Omega_0(\tau)T] I_\perp(\tau), \end{aligned} \tag{A.2}$$

where, we defined a function

$$\Omega_k(\tau) = 2\pi \int_0^1 x^{1-k} \mathrm{e}^{-(1/x-1)\tau}\,\mathrm{d}x, \tag{A.3}$$

and Ω_0 is the effective solid angle at the level t.

Let us divide the total exposure time T into small intervals $\Delta T_i = T/m$ $(i = 1, 2, \ldots, m)$, and put the altitude of balloon corresponding to ith interval as t_i $(= \tau_i \Lambda)$. Then, using Eq. (A.2), we get immediately the total number incident upon the detector during the exposure,

$$N_{\mathrm{obs}} = [S\bar{\Omega}T] I_\perp(\bar{\tau}). \tag{A.4}$$

Here,

$$\bar{\tau} = \frac{1}{m} \sum_{i=1}^{m} \tau_i, \tag{A.5a}$$

$$\bar{\Omega} = \frac{1}{m} \sum_{i=1}^{m} \Omega_0(\tau_i) \mathrm{e}^{-(\tau_i - \bar{\tau})}, \tag{A.5b}$$

are both evaluated from the actual flight record shown in Fig. 2, and $\bar{\Omega}$ depends slightly on the attenuation length Λ of the primary particle.

Now, from Eq. (A.4), we can obtain straightforwardly the absolute intensity I_0 at the top of the atmosphere without worrying about the altitude fluctuation of balloon. It is, however, quite complicated to apply the above procedure, dividing the exposure time into so many small intervals, for the practical data analysis, particularly for the atmospheric correction and the calculation of detection efficiency as shown in Appendix B.

In order to avoid such a complexity, we had better introduce an "effective" altitude t_e so that Eq. (A.4) is equal to Eq. (A.2). Namely we have to solve a following transcendental equation with respect to $t_e(=\tau_e\Lambda)$,

$$\Omega_0(\tau_e)e^{-\tau_e} = \bar{\Omega}e^{-\bar{\tau}}. \tag{A.6}$$

We can get t_e easily in the following way. As t_e is not greatly different from the average altitude $\bar{t}$, we can put

$$\tau_e = \bar{\tau} + \Delta\tau, \tag{A.7}$$

and expanding the left-hand side of Eq. (A.6) with respect to $\Delta\tau$ after substituting Eq. (A.7) into Eq. (A.6), we obtain a solution

$$\Delta\tau = [\Omega_0(\bar{\tau}) - \bar{\Omega}]/\Omega_1(\bar{\tau}), \tag{A.8}$$

where Ω_1 is defined by putting $k = 1$ in Eq. (A.3). If the approximation is not satisfactory, we repeat the same procedure after replacing $t_e(\equiv \bar{t} + \Delta t)$ by $\bar{t}$. Practically, however, even two or three iterations are enough.

In Table 5, we show the numerical values of the effective altitude thus estimated for four flights. Once we get the effective altitude t_e, we can estimate easily the atmospheric correction factor, $\alpha_c \equiv \exp(t_e/\Lambda)$. From this table, we find, for example, $\alpha_c = 1.08$ and 1.98 in the cases of proton and iron primaries, respectively.

Appendix B. Simulation calculation of the detection efficiency

One of the most important assumptions for the calculation of the detection efficiency is a type of model for the reaction cross-section σ_R. In this paper, we consider two typical models, hard-sphere model [56] and the soft-sphere model [57] for nucleus–nucleus interaction. The former model gives

$$\sigma_R = \pi r_0^2 \,(A_P^{1/3} + A_T^{1/3} - \kappa)^2. \tag{B.1}$$

Here, A_P (or A_T) is the mass number of projectile (or target) nucleus, and

$$r_0 = 1.29 \times 10^{-13} \text{ cm}, \tag{B.2a}$$

$$\kappa = 1.189 \exp[-0.05446 \ \min(A_P, A_T)]. \tag{B.2b}$$

This model has been used for the efficiency calculation in JACEE chamber [63].

On the other hand the latter model gives

$$\sigma_R = \pi(a_P^2 + a_T^2)[\ln\chi + \mathrm{Ei}(\chi) + \gamma], \tag{B.3}$$

$$\chi = \sigma_{NN}\frac{A_P A_T}{\pi(a_P^2 + a_T^2)}, \tag{B.4}$$

Table 5
Numerical values of effective altitude of RUNJOB balloon for typical primary elements

Primary charge	Attenuation length (g/cm^2)	Effective altitude (g/cm^2)			
		RUNJOB I	RUNJOB II	RUNJOB III	RUNJOB IV
1	110.00	11.60	11.21	12.02	12.25
2	48.68	11.23	10.84	11.60	11.85
8	26.68	10.96	10.55	11.28	11.51
14	20.64	10.84	10.41	11.12	11.36
20	17.14	10.74	10.29	10.99	11.23
26	14.97	10.67	10.21	10.89	11.14

where, γ ($= 0.5772$) is the Euler constant, Ei(χ) is the integral exponential function, and σ_{NN} is the cross- section for the nucleon–nucleon interaction including energy dependence, and a_P (or a_T) is related to the nuclear root-mean-square radius of the projectile (or target) nucleus (see Ref. [57] for detail).

In the case of proton–nucleus interaction, we use a cross-section based on the soft-sphere model including the energy dependence, which is in good agreement with that proposed by Hillas [58].

In Fig. 20, we demonstrate the collision lengths λ_c expected from the above two models for typical projectiles and targets. One finds, for instance, the former length gives 10–20% higher than the latter length in the energy region of our interest, ~100 TeV, in the case of helium projectile, namely the detection efficiency based on the former model is 10–20% less than that based on the latter model. In the present paper, we use the soft-sphere model for the practical estimation of the absolute intensities as shown in Section 4.

Before going to the details of the simulation procedure, we illustrate a top view and a side view of our detector in Fig. 21. The detector consists of two chambers, A and B, and its area S is 50×80 cm^2, and the geometrical height of the module h is 38.3 cm (21.1 cm) for 1995 (1996) chamber. The shield box is made of the black acrylic plate with the side thickness of 1.2 cm (1.3 cm) for 1995 (1996) chamber, and with the top-cover thickness of 1.0 cm for 1996 chamber, whereas the top cover of 1995 chamber is made of a luan with the thickness of 1.5 cm. All of these numerical parameters

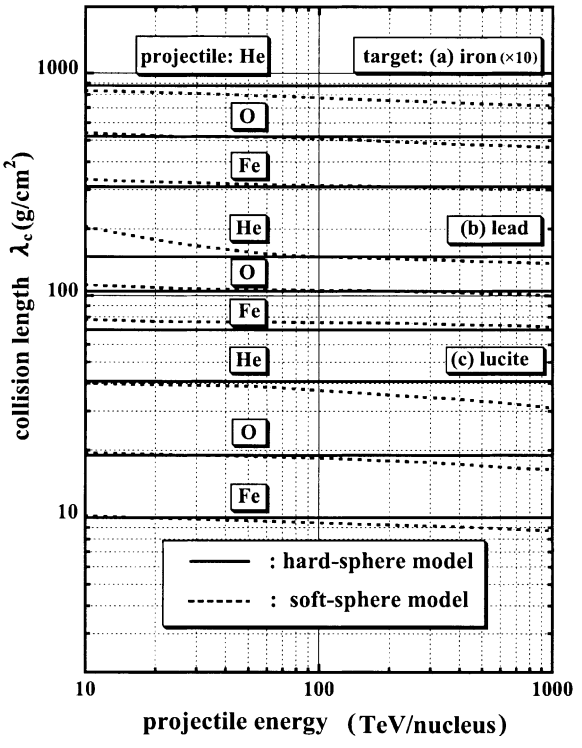

Fig. 20. Collision length expected from two models, the soft-sphere model and the hard-sphere model for typical projectiles and targets, where λ_c is multiplied by ten in the case of iron target to discriminate from the other curves.

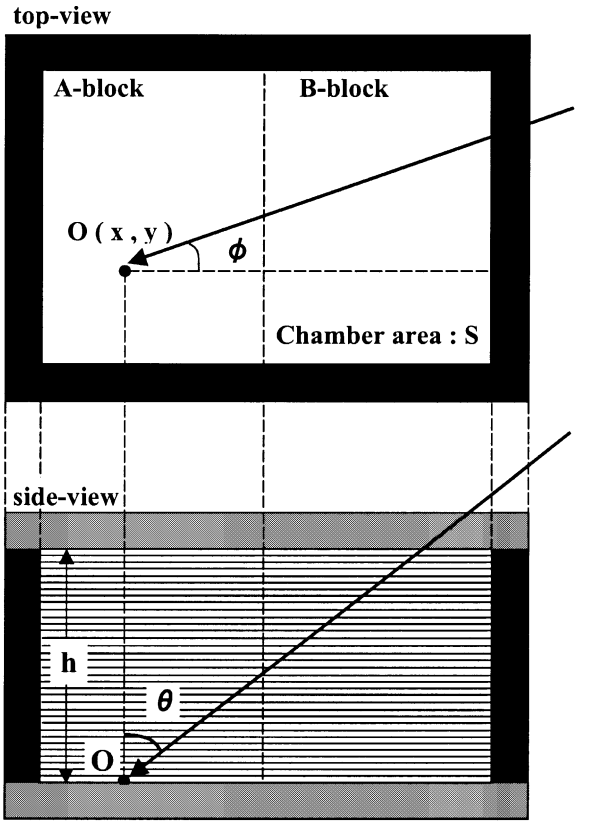

Fig. 21. View of our chamber configuration, and the feature of cosmic rays trajectory.

are exactly taken into account in the present calculation.

Let us consider a cosmic-ray particle incident upon the bottom of module at a position, $O(x,y)$, from a direction, (θ,ϕ). The number of the cosmic-ray particle ΔN arriving at a small area, $\Delta S = \Delta x\Delta y$, within a small solid angle, $\Delta\Omega = \Delta\cos\theta\Delta\phi$, is immediately written down from Eq. (A.2) in Appendix A as

$$\Delta N = I_0[\Delta S\Delta\Omega T]\cos\theta e^{-t_e/\Lambda\cos\theta}, \tag{B.5}$$

where T is the exposure time, Λ is the attenuation length of the cosmic-ray primary, and t_e is the effective altitude of a balloon. As discussed in Appendix A, we do not need to worry about the altitude fluctuation of the balloon now, once we get the effective altitude t_e. We replace t_e into t in the following discussion for the sake of simplicity.

Now, we touch upon briefly the criterion of event selection for those recorded successively on multi-sheets of the X-ray film in the form of dark spot, which is quite essential for the calculation of the detection efficiency.

The dark spot is formed on the X-ray film due to the electromagnetic cascade shower originated in the nuclear interaction at target (or lead plate in the calorimeter). It is visible by naked-eye if the net optical darkness D_{net} is larger than $\sim$0.1 after subtracting the background spot-darkness D_{bg} (see Eqs. (B.11a) and (B.11b)). So, we select only events satisfying a condition that shower spots with $D_{net} \geqslant 0.1$ are observed on more than two sheets of X-ray film inserted in the calorimeter.

We set further an additional condition that the path length from a VP to a bottom point is more than 4 c. u., which rejects a jet event occurring near the bottom of the lower calorimeter.

Let us put the detection probability as $P(x,y;\ \theta,\phi)$ for the case of the cosmic-ray trajectory shown in Fig. 21, which includes the above two conditions as well as a collision probability and the geometry of the trajectory. Then, from Eq. (B.5), we obtain the number of cosmic rays actually observed,

$$\begin{aligned} N_{obs} &= \int\cdots\int P(x,y;\ \theta,\phi)\Delta N \\ &= [\xi S\Omega_0(\tau)T]I_0 e^{-\tau} \quad \text{with } \tau = t/\Lambda, \end{aligned}$$

leading to

$$I_0 = \frac{1}{[\xi S\Omega_0(\tau)T]e^{-\tau}}\ N_{obs}, \tag{B.6}$$

here,

$$\begin{aligned} \xi = \frac{1}{S\Omega_0(\tau)} &\int\int_S dx\,dy \int\int_{\Omega\leqslant 2\pi} d\cos\theta\,d\phi \\ &\times P(x,y;\ \theta,\phi)\cos\theta e^{-(\sec\theta-1)\tau}, \end{aligned} \tag{B.7}$$

is nothing but the detection efficiency we need. Once we get it, we can estimate the absolute intensity I_0 straightforwardly from the observed number N_{obs} with use of Eq. (B.6).

As the practical form of $P(x,y;\ \theta,\phi)$ is, however, very complicated, we calculate ξ with use of the simulation method in following steps.

Step 1: Sampling of a primary energy E_0 according to the familiar power form, $\propto E_0^{-\beta}$. Explicit numerical value β is summarized in Table 3 in the text.

Step 2: Uniform sampling of a position of the particle, (x,y), incident upon the bottom layer.

Step 3: Sampling of an incident direction, (θ,ϕ), according to the following distribution function,

$$F(\theta,\phi)d\cos\theta\,d\phi = \cos\theta e^{-(\sec\theta-1)\tau}\ \frac{d\cos\theta\,d\phi}{\Omega_0(\tau)}, \tag{B.8}$$

which is the integrand of Eq. (A.2). If $\tan\theta > 5.0$, we go to Step 1.

Step 4: Sampling of a VP according to the cross-section given by Eqs. (B.1) and (B.2). If the nuclear collision occurs either outside the chamber or at the shield box, we go to Step 1.

Step 5: If the path length from the VP to the position, (x,y), at the bottom layer is less than 4 c.u., we go to Step 1.

Step 6: Sampling of secondary particles produced by the nuclear collision with the use of FRITIOF code. For a surviving proton and/or a

fragment nucleus (including nucleons) due to the nucleus–nucleus collision, we repeat the Step 4 for each particle.

Step 7: γ-rays thus produced are linked to the simulation code for the pure electromagnetic cascade shower, applicable even for the heterogeneous chamber structure [35].

We calculate simultaneously the darkness of each shower spot with use of the characteristic curve of X-ray film [45], i.e., the electron density ρ(no./cm^2) vs. optical darkness D (in half side emulsion coated on the X-ray film) given by

$$D(\rho) = D_0\left[1 - \frac{1}{1+\alpha\rho}\right], \tag{B.9}$$

where

$$D_0 = 6.5 \quad \text{and} \quad \alpha = 5.50 \times 10^{-8}\ \text{cm}^2. \tag{B.10}$$

The net spot darkness D_{net} within the slit size of $300 \times 300\ \mu\text{m}^2$ is calculated, taking into account the inclination effect, by

$$D_{\text{net}} = D_{\text{u}} + D_{\text{d}}, \tag{B.11a}$$

where

$$D_{\text{u,d}} = D(\rho_{\text{u,d}} + \rho_{\text{bg}}) - D(\rho_{\text{bg}}), \tag{B.11b}$$

and $\rho_{\text{u}}(\rho_{\text{d}})$ is the electron shower density at upper(lower) emulsion surfaces of X-ray film, and ρ_{bg} is a background density, which is estimated back from Eq. (B.9) with use of the observed background D_{bg} on half side emulsion, for instance $D_{\text{bg}} = 0.58$ in the case of RUNJOB 1996.

If shower spots with $D_{\text{net}} \geqslant 0.1$ are observed on more than two sheets of X-ray film, we go to Step 8, or else go to Step 1.

Step 8: Sampling of $\epsilon_\gamma \equiv \Sigma E_{\gamma,\text{esti}}$, according to the Gaussian form, $\propto \exp[-Y^2/2\sigma^2]$ with $Y = \log_{10}[\epsilon_\gamma/\epsilon_{\gamma,0}]$, where $\epsilon_{\gamma,0} \equiv \Sigma E_{\gamma,\text{true}}$ is the energy sum obtained by the Step 6, and $\sigma = 0.13$–0.16 depending on the kind of primary (see Fig. 10 in the text). If $\epsilon_\gamma \leqslant 1$ TeV, we go to Step 1, or else count the number of events, $N(\epsilon_\gamma) = N(\epsilon_\gamma) + 1$, and go to Step 1.

After converting from ϵ_γ into E_0 with use of the conversion factor summarized in Table 3 in the text (see also Appendix D), finally we obtain the detection efficiency,

$$\xi(E_0) = \frac{N(E_0)}{N_0(E_0)}, \tag{B.12}$$

where $N_0(E_0)$ is the initial number of particles incident upon the chamber bottom for the *true* primary energy, and $N(E_0)$ is the observed one, taking the detection condition into account. Numerical results are presented in Fig. 6 in the text.

Appendix C. Threshold energy effect in the energy determination

In EC with target module, we face inevitably with the following two restrictions in detection of γ-core produced by a local nuclear interaction occurred in the target,

$$E_\gamma \gtrsim E_{\text{c}} \quad \text{and} \quad r_\gamma \lesssim r_{\text{c}}, \tag{C.1}$$

where E_γ is the γ-core energy, and r_γ is the distance from the energy-weighted centre of γ-core's at the plane of target diagram. For instance, in RUNJOB experiment,

$$E_{\text{c}} = 50\text{–}100\ \text{GeV}, \tag{C.2a}$$

and

$$r_{\text{c}} = 0.5\text{–}1\ \text{mm}. \tag{C.2b}$$

The average height of the VP being $\sim$20 cm, we have a cut-off emission angle,

$$\theta_{\text{c}} = 2.5\text{–}5.0 \times 10^{-3}\ \text{rads}. \tag{C.2c}$$

Eqs. (C.2a) and (C.2c) are, however, not independent, but closely connected with each other in the following form

$$\theta_{\text{c}} \simeq \frac{\langle p_t \rangle}{E_{\text{c}}}. \tag{C.3}$$

For instance, putting $E_{\text{c}} = 50$ GeV and $\langle p_t \rangle = 200$ MeV/c, we get

$$\theta_{\text{c}} \simeq 4 \times 10^{-3}\ \text{rads},$$

giving a result consistent with Eq. (C.2c).

Now, we have to modify Eqs. (10a)–(10c) in the text, taking into account the threshold energy effect mentioned above. To make the calculation easier, we assume a trial model, where a fireball decays isotropically into γ-rays that carry the most part of ΣE_γ.

The distribution function is supposed to be of the following form in the fireball rest system

$$\psi(\epsilon^*,\theta^*)\,\mathrm{d}\epsilon^*\,\mathrm{d}\Omega^* = n_0 \mathrm{e}^{-\epsilon^*/\epsilon_0}\,\frac{\mathrm{d}\epsilon^*}{\epsilon_0}\,\frac{\mathrm{d}\Omega^*}{4\pi}, \tag{C.4}$$

where n_0 is the average γ-ray multiplicity, and ϵ_0 is the average energy of γ-ray in the fireball rest system, approximately equal to p_0 appeared in Eq. (4) in the text.

Then, we obtain a following energy-angular distribution of γ-rays in the laboratory system,

$$\psi(E_\gamma,\theta)\mathrm{d}E_\gamma\,\mathrm{d}\theta = n_0 \mathrm{e}^{-z}\,\mathrm{d}x\frac{\mathrm{d}z}{z}, \tag{C.5}$$

where

$$x = \frac{1}{2}\,\frac{n_0 E_\gamma}{\Sigma E_\gamma} = \frac{1}{2}\,\frac{E_\gamma}{\langle E_\gamma\rangle}, \tag{C.6a}$$

and

$$z = x(1+y^2) \quad \text{with} \quad y = \theta\langle E_\gamma\rangle/\epsilon_0. \tag{C.6b}$$

ΣE_γ appeared in Eq. (C.6a) is the shower energy transferred by the fastest moving fireball for $E_\mathrm{c} = 0$ and $\theta_\mathrm{c} = \infty$. Integrating over x and $y(z)$ in Eq. (C.5), we find a familiar form for the angular and the energy distribution respectively,

$$n_0\frac{\mathrm{d}y^2}{(1+y^2)^2}, \tag{C.7a}$$

and

$$n_0 \mathrm{E}_1(x)\,\mathrm{d}x, \tag{C.7b}$$

namely the former gives a well-known isotropic angular distribution and the latter an exponential integral energy distribution, which are both consistent with the experimental data in the forward region [38,39,59,60].

Now, we calculate the average energy including the threshold energy effect, with use of Eq. (C.5),

$$\langle E_\gamma\rangle_\mathrm{c} = \frac{\int_0^{\theta_\mathrm{c}}\mathrm{d}\theta\int_{E_\mathrm{c}}^{\infty} E_\gamma\psi(E_\gamma,\theta)\,\mathrm{d}E_\gamma}{\int_0^{\theta_\mathrm{c}}\mathrm{d}\theta\int_{E_\mathrm{c}}^{\infty}\psi(E_\gamma,\theta)\,\mathrm{d}E_\gamma}. \tag{C.8}$$

The explicit form of Eq. (C.8) is given by

$$\langle E_\gamma\rangle_\mathrm{c} = \omega_\mathrm{c}\langle E_\gamma\rangle + E_\mathrm{c}, \tag{C.9}$$

where

$$\omega_\mathrm{c} = \frac{G_3(x_\mathrm{c},z_\mathrm{c})}{G_2(x_\mathrm{c},z_\mathrm{c})}, \tag{C.10}$$

and

$$G_k(x,z) = (k-1)x^{k-1}\int_x^z \frac{\mathrm{e}^{-v}}{v^k}\,\mathrm{d}v. \tag{C.11}$$

Two parameters, x_c and z_c, are given by replacing E_γ and θ into E_c and θ_c respectively in Eqs. (C.6a) and (C.6b).

On the other hand, from Eq. (6) in the text, $\langle E_\gamma\rangle_\mathrm{c}$ is obtained experimentally by

$$\langle E_\gamma\rangle_\mathrm{c} \simeq \frac{1}{n_\mathrm{c}}\sum_{i=1}^{n_\mathrm{c}}\frac{\langle p_t\rangle(\theta_i,E_\mathrm{c})}{\theta_i}, \tag{C.12}$$

where n_c is an observed multiplicity for $E_\gamma \geqslant E_\mathrm{c}$ and $\theta \leqslant \theta_\mathrm{c}$, and connected with n_0 in the following relation with use of Eq. (C.11),

$$n_\mathrm{c} = n_0 G_2(x_\mathrm{c},z_\mathrm{c}). \tag{C.13}$$

Finally, from Eqs. (4) and (6) in the text and Eqs. (C.9) and (C.12), we find the same equation as Eqs. (10a)–(10c) in the text, after re-defining $f(u)$ in Eq. (8b) as,

$$f(u) = \frac{1}{\omega_\mathrm{c}}\,\frac{p_0}{q_0}\,\frac{1-\mathrm{e}^{-u}}{u}. \tag{C.14}$$

Now, after solving the modified transcendental equations simultaneously with respect to $(\langle E_\gamma\rangle\ ;\ x_\mathrm{G}, y_\mathrm{G})$, we obtain n_0 from Eqs. (C.13), (C.6a), (C.6b) and (C.11). Finally we can get effective shower energy, $\Sigma E_\gamma = n_0\langle E_\gamma\rangle$, taking into account the cut-off effect, $E_\gamma \geqslant E_\mathrm{c}$ and $\theta \leqslant \theta_\mathrm{c}$.

To apply the iteration method, we need an initial set of $(\langle E_\gamma\rangle;\ x_\mathrm{G}, y_\mathrm{G})$, and in practice, we put initially

Table 6
Numerical values of parameters appeared in Eqs. (C.16a) and (C.16b) and the scale-shift factor discussed in Section 3.2

	$\hat{p}_0$ (MeV/c)	$\hat{q}_0$ (MeV)	μ	ν_p	ζ	ν_q	S_{shift}
Proton	170	72.0	0.075	4.0	1.15	2.50	1.12
Helium	170	85.0	0.062	6.0	1.15	2.50	1.15
Iron	170	68.0	0.060	6.0	1.15	2.50	1.29

$$\langle E_\gamma \rangle = \frac{1}{n_c} \sum_{i=1}^{n_c} \frac{p_0}{\theta_i}, \tag{C.15a}$$

$$x_G = \frac{1}{n_c} \sum_{i=1}^{n_c} x_i, \quad \text{and} \quad y_G = \frac{1}{n_c} \sum_{i=1}^{n_c} y_i, \tag{C.15b}$$

where θ_i is estimated by the use of the above initial centre of axis, (x_G, y_G), and n_c is the observed γ-ray multiplicity. Of course, these values are iteratively changed into new ones.

In Section 3.2, we assumed two parameters, p_0 and q_0, are independent of the shower energy ΣE_γ as well as the (effective) multiplicity n_0. By fitting Eqs. (4) and (5) carefully into the data, we find that the following forms reproduce well the correlation of $\langle p_t \rangle(\theta) - \theta$ in both C-jet data and FRITIOF simulational data.

$$p_0 = \hat{p}_0 \ (1 - e^{-n_0/\nu_p})[\Sigma E_\gamma]^\mu, \tag{C.16a}$$

and

$$q_0 = \hat{q}_0 \ (1 + \zeta e^{-n_0/\nu_q}). \tag{C.16b}$$

Explicit numerical values appeared in Eqs. (C.16a) and (C.16b) are summarized in Table 6, where S_{shift} denotes the scale-shift factor discussed in Section 3.2.

Appendix D. Conversion of $\sum E_\gamma$ into E_0

In Section 3, we show that the shower energy ΣE_γ is determined satisfactorily with the use of γ-core, and the accuracy is nearly comparable with that of the energy estimated by the photometric method. Now, the problem is about the conversion of ΣE_γ into the primary energy E_0. This is closely connected to the inelasticity k_γ, transferred into γ-ray component produced in the nuclear interaction. Therefore, it is a natural claim that the conversion into E_0 is hard to determine for individual showers, since the distribution of k_γ is rather broad, particularly in the case of iron as shown in Fig. 22 (filled circle).

However, all we have to do for the practical purpose is to find an *effective* conversion factor C_γ $(\equiv E_0/\Sigma E_\gamma)$ so that the *true* E_0-spectrum is reproduced from ΣE_γ-spectrum we actually observe, no matter if each conversion may fluctuate considerably.

From a simple calculation, we get the following relation [45], assuming a power spectrum with index B $(= \beta - 1)$ in integral E_0-spectrum,

$$C_\gamma = 1/[\langle k_\gamma^B \rangle]^{1/B}, \tag{D.1}$$

where

$$\langle k_\gamma^B \rangle = \int_0^1 x^B \phi(x)\, dx, \tag{D.2}$$

and ϕ is a distribution function of k_γ.

Nevertheless, one may argue that the above procedure, shifting ΣE_γ-spectrum to E_0-spectrum by multiplying C_γ, is allowable only for proton component with large statistics, and it does not work for heavier ones with small statistics, particularly for iron element, where the fluctuation of k_γ might become serious.

We have to point out, however, on an important detection condition inherent in the EC experiment, namely an event with small k_γ corresponds to small shower energy on average, and then practically it is lost in the initial stage of naked-eye scanning on X-ray films, since the dark-spot signal is too thin to observe by naked-eye. This detection condition cuts the tail of small k_γ, and makes the spread of k_γ-distribution much narrower than that of the original one.

Let us compare explicitly two k_γ distributions normalized by $\langle k_\gamma \rangle$ in Fig. 22, one (filled circle) from the original without any detection bias and

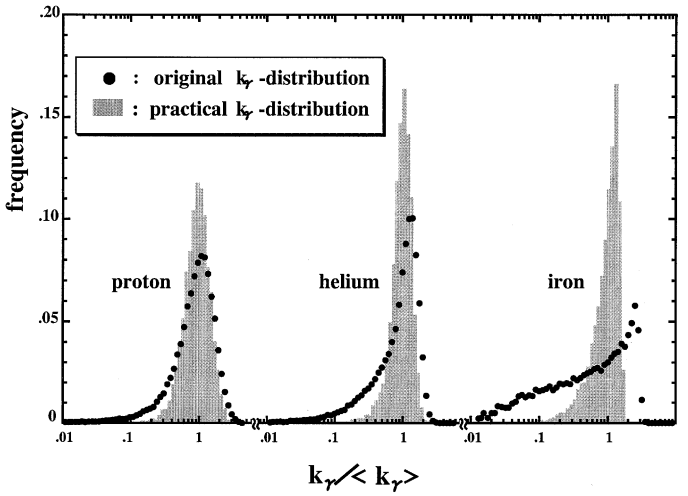

Fig. 22. Normalized k_γ-distributions for two selection conditions; without any selection criterion (•), i.e., original k_γ-distribution and with the selection condition (grey histogram) mentioned in Appendix C.

the other (grey histogram) from the practice taking the actual event selection into account (see Appendix B), where three typical elements, proton, helium and iron, are demonstrated in the case of cal. jet. As mentioned before, we find that the spread of the k_γ distribution we actually observe (grey histogram) is significantly reduced in comparison with the original one (filled circle). Therefore, we can apply the conversion procedure mentioned here also for heavy-initiated shower.

The conversion factor appeared in Eq. (D.1) is calculated with use of the FRITIOF code, taking into account the successive interactions in chamber, though it is not so effective in our chamber due to the thin type calorimeter. In Table 3 in the text, we summarize the conversion factor for typical primary elements, which are nearly consistent with the past works. For instance, we show those obtained by JACEE [63], MUBEE [23] and SANRIKU [45] in Table 7 for typical elements. Small difference between our results in Table 3 and those in Table 7 come from the different chamber structure, and then they are rather in good agreement with one another, taking this effect into account.

Now, we would like to mention that the present procedure in estimating C_γ is absolutely based on the assumption of energy-independent k_γ-distribution. Then, if it depends on the primary energy E_0, the numerical values summarized in Table 3 are not applicable for the conversion into E_0.

Though we have no direct evidence for the energy independence of the k_γ-distribution in the higher energy region $E_0 \gtrsim 10$ TeV, it is well known that the attenuation lengths of both hadronic (mostly nucleons) and electromagnetic components in the atmosphere do not change very significantly with interaction energy [61], and have

Table 7
C_γ estimated by JACEE, MUBEE and SANRIKU in the case of calorimeter jet

	Proton ($\beta = 2.8$)	Helium ($\beta = 2.8$)	C, N, O ($\beta = 2.7$)	Ne, Mg, Si ($\beta = 2.7$)	Iron ($\beta = 2.6$)
JACEE	3.64	5.10	7.04	7.58	9.09
MUBEE	4.00	5.88	8.62	9.43	11.1
SANRIKU	3.89	5.61	7.63	9.26	10.2

Table 8
Average inelasticity $\langle k_\gamma \rangle$ without any detection bias expected from several simulation codes

Target	Model	Projectile			
		Proton	Helium	Oxygen	Iron
Carbon:	FRITIOF	0.199	0.105	0.054	0.026
	VENUS	0.183	0.092	0.048	0.030
	QGSJET	0.194	0.091	0.047	0.026
Iron:	FRITIOF	0.208	0.134	0.092	0.054
	VENUS	0.189	0.117	0.088	0.059
	QGSJET	0.208	0.114	0.078	0.044
Lead:	FRITIOF	0.217	0.164	0.125	0.080
	VENUS	0.198	0.138	0.110	0.089
	QGSJET	0.219	0.145	0.108	0.075

a constant value ($\simeq$100 g/cm^2) within the energy range of our interest. This is closely connected to the inelasticity and the collision cross-section. So, our assumption is not far from the actual evidence, though based on the indirect observational data.

One may argue further that these studies might depend on the model of nuclear interaction. This is also not so serious obstacle for our purpose, since only k_γ is the principal parameter, and the difference in the production spectrum of the energy and the emission angle for individual γs among various models is the second order effect, as far as the conversion-factor problem is concerned.

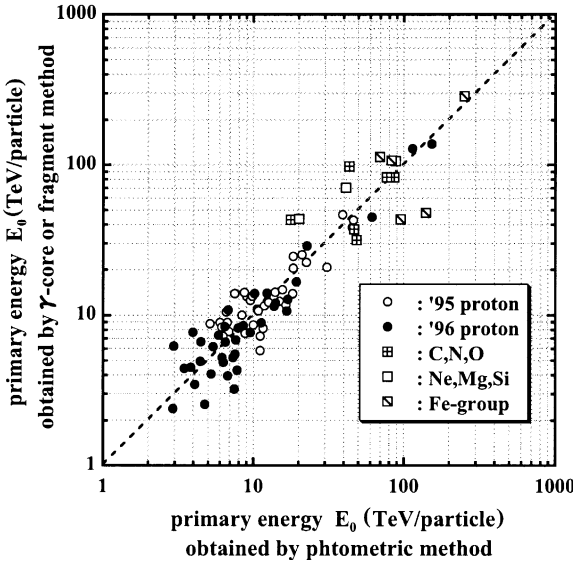

Fig. 23. Scatter plot of the heavy-primary energies obtained by two methods, $E_0^{(\mathrm{frag})}$ and $E_0^{(\mathrm{photo})}$. Proton-primary events are also plotted for reference, where their primary energies are obtained by multiplying the conversion factor and the shower energies shown in Fig. 11.

In Table 8, we summarize the average value of inelasticity $\langle k_\gamma \rangle$ (without any detection bias), expected from several simulation codes (CORSIKA [62]) for typical projectiles and targets. One finds the difference is not so significant among individual models, and must be masked behind the resolution of the present energy determination (see Section 3 in the text).

Now, as mentioned in the beginning of Section 3.2, we can estimate independently the primary energy $E_0^{(\mathrm{frag})}$ with use of the emission angle of fragments such as p, $\alpha, \ldots$, produced by the break up of heavy primary. So we compare it with the primary energy $E_0^{(\mathrm{photo})}$ obtained by the conversion of ΣE_γ into E_0, using Table 3.

In Fig. 23, we demonstrate the correlation between these two energies for heavy primaries, where proton events are also plotted for reference, which are obtained by converting ΣE_γ in Fig. 11 into E_0 with the use of Table 3. We find the dispersion appeared in $E_0^{(\mathrm{frag})}$ vs. $E_0^{(\mathrm{photo})}$ is somewhat larger than those in $E_0^{(\mathrm{core})}$ vs. $E_0^{(\mathrm{photo})}$.

In the present paper, however, we do not use $E_0^{(\mathrm{frag})}$ for heavy primary, but use $E_0^{(\mathrm{photo})}$ and/or $E_0^{(\mathrm{core})}$, because the emission angle of fragment products (p, He, ...) is hard to measure in the 1996 chamber as mentioned in the beginning of Section 3.2.

References

[1] K. Greisen, Phys. Rev. Lett. 16 (1966) 748.
[2] G.T. Zatsepin, V.A. Kuzmin, Pisma Zh. Eksp. Theor. Fiz. 4 (1966) 114.
[3] G.V. Kulikov, G.B. Khristiansen, Sov. Phys. JEPT 35 (1959) 441.
[4] B. Peters, Suppl. Nuovo Cimento 14 (1959) 436.
[5] G.F. Krimsky, Dokl. Akad. Nauk SSSR 234 (1977) 1306.
[6] W.I. Axford, E. Leer, G. Skadon, Proc. 15th Int. Cosmic Ray Conf., vol. 11, Provdiv, Bulgaria, 1977, p. 132.
[7] R.D. Blandford, J.P. Ostriker, Astrophys. J. L29 (1978) 221.
[8] A.R. Bell, Proc. 22nd Int. Cosmic Ray Conf., vol. 2, Dublin, Ireland, 1991, p. 420.
[9] W.I. Axford, Suppl. Astrophys. J. 90 (1994) 937.
[10] J. Wdowczyk, A.W. Wolfendale, J. Phys. A. 6 (1973) 1594.
[11] T.K. Gaisser, in: M. Nagano, F. Takahara, (Eds.), Astrophysical Aspects of the Most Energetic Cosmic Rays, Singapore, World Scientific, 1991, p. 146.
[12] R.J. Protheroe, A.P. Szabo, Phys. Rev. Lett. 69 (1992) 2885.
[13] R.J. Jokipii, G. Morfill, Astrophys. J. 312 (1987) 170.
[14] V.S. Ptuskin, in: M. Nagano, F. Takahara, (Eds.), Astrophysical Aspects of the Most Energetic Cosmic Rays, Singapore, World Scientific, 1991, p. 112.
[15] V.S. Ptuskin, et al., Astron. Astrophys. 268 (1992) 726.
[16] S.I. Nikolsky, Proc. in: Y. Fujimoto (Ed), Eigth Int. Symp. Very High Energy C. R. Int., 1994, p. 267.
[17] Y. Muraki, Proc. 21st Int. Cosmic Ray Conf., vol. 11, Adelaide, Australia, 1990 p. 257.
[18] M. Ichimura, et al., Phys. Rev. D 48 (1993) 1949.
[19] JACEE collaboration, Proc. 25th Int. Cosmic Ray Conf., vol. 4, Durban, South Africa, 1997, p. 1.
[20] JACEE collaboration, Astrophys. J. 502(1998) 278.
[21] I.P. Ivanenko, et al., Proc. 23rd Int. Cosmic Ray Conf., vol. 2, Calgary, Canada, 1993, p. 17.
[22] S.P. Swordy, et al., Astrophys. J. 403 (1993) 658.
[23] V.I. Zatsepin, et al., Yad. Fiz. 57 (1994) 684.
[24] A. Nakamura, Master Thesis, Aoyama-Gakuin University, 1995.
[25] E. Kamioka, et al., Astrop. Phys. 6 (1997) 155.
[26] J. Nishimura, in: S. Flugger (Ed.), Handbuch der Physik, Springer, Berlin, 46/2 (1967) 1.
[27] I.P. Ivanenko, et al., Nauka (1980) 306.
[28] M. Okamoto, T. Shibata, Nucl. Instr. Meth. A 257 (1987) 155.
[29] M. Ichimura, et al., Nucl. Instr. Meth. A 300 (1991) 374.
[30] M. Ichimura, Ph.D. Thesis, Aoyama-Gakuin University, 1992.
[31] J. Nishimura, T. Kobayashi, Y. Komori, K. Yoshida, Adv. Space Res. 19 (1997) 767.
[32] A.V. Apanasenko, et al., Proc. 25th Int. Cosmic Ray Conf., vol. 5, Durban, South Africa, 1997, p. 301.
[33] A.V. Apanasenko, et al., Proc. 25th Int. Cosmic Ray Conf., vol. 5, Durban, South Africa, 1997, p. 13.
[34] M. Ichimura, K. Kirii, T. Shibata, Nucl. Instr. Meth. A 300 (1991) 616.
[35] T. Fujinaga, M. Ichimura, Y. Niihori, T. Shibata, Nucl. Instr. Meth. A 276 (1989) 317.
[36] N. Hotta, et al., Phys. Rev. D 22 (1980) 1.
[37] Y. Sato, H. Sugimoto, Proc. 16th Int. Cosmic Ray Conf., vol. 7, Kyoto, Japan, 1979, p. 42.
[38] C.M.G. Lattes, Y. Fujimoto, S. Hasegawa, Phys. Rep. 65 (1980) 151.
[39] Brasil–Japan Emulsion Chamber Collaboration, ICR-Report-91-81-7, Institute for Cosmic Ray Research, University of Tokyo, 1981.
[40] D.S. Oshuev, Ph.D. Thesis, Moscow State University, 1998.
[41] S. Kuramata, et al., reprint: INP Moscow State University, 44/496, 1997.
[42] H. Nanjo, et al., Proc. Balloon Symp. Mimeographed Circular in Japanese, Institute of Space and Astronautical Science, Sagamihara, Japan, 1995, p. 147.
[43] E. Pare, et al., Phys. Lett. B 242 (1990) 531.
[44] P. Hong, Comp. Phys. Commun. 71 (1992) 173.
[45] Y. Kawamura, et al., Phys. Rev. D 40 (1989) 729.
[46] M.J. Ryan, J.F. Ormes, V.K. Balasubrahmanyan, Phys. Rev. Lett. 28 (1972) 985.
[47] A.A. Watson, A.W. Wolfendale, in: M. Nagano, F. Takahara (Eds.), Astrophysical Aspects of the Most Energetic Cosmic Rays, Singapore, World Scientific, 1991, p. 61.
[48] W. Menn, et al., Proc. 25th Int. Cosmic Ray Conf., vol. 3, Durban, South Africa, 1997, p. 409.
[49] D.E. Ellision, Proc. 23rd Int. Cosmic Ray Conf., vol. 2, Calgary, Canada, 1993, p. 219.
[50] T. Shibata, Phys. Rev. D 22 (1980) 100.
[51] R.W. Ellsworth, G.B. Yodh, T.K. Gaisser, in: T.K. Gaisser (Ed.), Proc. of Bartol Conf., AIP, New York, 1979, p. 111.
[52] N.L. Grigorov, et al., Proc. 12th Int. Cosmic Ray Conf., vol. 5, Tasmania, Australia, 1971, 1746, 1752, 1760.
[53] T. Shibata, Rapporteur talk at 24th Int. Cosmic Ray Conf., vol. 19C, (Rome, Italy), IL Nuovo Cimento, 1996, 713.
[54] M. Amenomori et al., Proc. 25th Int. Cosmic Ray Conf., vol. 2, Rome, Italy, 1995, p. 736.
[55] V.S. Ptuskin, et al., Astron. Astrophys. 268 (1993) 726.
[56] F.A. Hargen, et al., Astrophys. J. 212 (1977) 262.
[57] P.J. Karol, Phys. Rev. C 11 (1975) 1203.
[58] A.M. Hillas, Proc. 16th Int. Cosmic Ray Conf., vol. 6, Kyoto, Japan, 1979, p. 13.
[59] D.H. Perkins, P.H. Fowler, Proc. R. Soc London A 218 (1964) 401.
[60] G. Neuhofer, et al., Phys. Lett. 38B (1972) 51.
[61] E. Konishi, T. Shibata, E.H. Shibuya, N. Tateyama, Prog. Theor. Phys. 56 (1976) 1845.
[62] D. Heck, et al., Forschungszentrum Karlsruhe FZKA 6019 (1998).

[63] E.D. Olson, Ph.D. Thesis, University of Washington, 1995.
[64] N.L. Grigorov, et al., Izvestia Acad. Nauk SSSR Phys. Ser. 35 (1971) 2443.
[65] A.A. Watson, Rapporteur Paper, Proc. 25th Int. Cosmic Ray Conf., vol. 8, Durban, South Africa, 1997, p. 257.
[66] S. Yoshida, Rapporteur Paper, Proc. 26th Int. Cosmic Ray Conf., vol. 8, Salt Lake City, USA, 1999, p. 180.